

Doctoral Dissertations and Master's Theses

Spring 5-8-2023

Online Estimation of Unknown Parameters for Flexible Spacecraft

Nicolo Woodward
woodwarn@my.erau.edu

Follow this and additional works at: <https://commons.erau.edu/edt>



Part of the [Navigation, Guidance, Control and Dynamics Commons](#)

Scholarly Commons Citation

Woodward, Nicolo, "Online Estimation of Unknown Parameters for Flexible Spacecraft" (2023). *Doctoral Dissertations and Master's Theses*. 740.

<https://commons.erau.edu/edt/740>

This Thesis - Open Access is brought to you for free and open access by Scholarly Commons. It has been accepted for inclusion in Doctoral Dissertations and Master's Theses by an authorized administrator of Scholarly Commons. For more information, please contact commons@erau.edu.

By

A Thesis Submitted to the Faculty of Embry-Riddle Aeronautical University

In Partial Fulfillment of the Requirements for the Degree of

Master of Science in Aerospace Engineering

Embry-Riddle Aeronautical University

Daytona Beach, Florida

By

THESIS COMMITTEE

Graduate Program Coordinator,
Dr. Hever Moncayo

Date

Dean of the College of Engineering,
Dr. James W. Gregory

Date

Associate Provost of Academic Support,
Dr. Christopher Grant

Date

ACKNOWLEDGMENTS

I could not have undertaken this journey without the constant support of my mentor and chair of my committee Dr. Riccardo Bevilacqua who has been mentoring me for the last three years in which I have gathered rich experience in spacecraft design and testing. My deepest appreciation goes to my parents and my sister for their moral and financial support. They never stopped believing in my dreams and never will. Special thanks go to my girlfriend and my friends for their last-minute editing help and keeping my spirit to pursue my goals high during this journey; I am grateful to have them by my side. I am also grateful to have been mentored by Dr. Andrew Sinclair during AFRL Summer Scholars because of his invaluable feedback and knowledge. Thanks should also go to the Air Force Office of Scientific Research for the opportunity given me in pursuing this investigation and financial funding to accomplish it. The research work presented is currently sponsored under AFOSR Grant #FA9550-22-1-0104.

ABSTRACT

Attitude controls methods of highly flexible spacecraft have seen increased interest over the last decades thanks to the technological development of flexible solar panels and deployables, which improves the capabilities of small satellites. However, a high-fidelity model of the flexible mode dynamics is hard to obtain in on-ground testing because not all modes of frequencies can be observed, complicating the controller design. Furthermore, plastic deformations due to long periods of storage of stowed flexible components could result in exciting frequencies outside of the designed controller's bandwidth, leading to an uncontrollable system. This thesis proposes a method to develop a high-fidelity model of a spacecraft with a flexible appendage subject to large deformations by modeling it as a finite series of rigid links connected by torsional springs and dampers. To overcome the uncertainties in the flexible dynamics, an onboard estimation through an adaptive controller is performed for these unknowns while the spacecraft is maneuvered. The controller uses integral concurrent learning (ICL), an adaptive scheme that records inputs and outputs provided by sensors mounted on the flexible body. The novelty of this investigation is the development of self-adapting control gains for both the tracking error and the learning matrix obtained from ICL. After tuning the controller for the system's initial conditions, it achieves the objective of tracking a desired trajectory while accurately learning the unknown physical parameters of the flexible appendage by only using the recorded measurements. It was observed that for a finer discretization of the flexible appendage and therefore a higher fidelity model of the flexible dynamics, the estimation algorithm is able to observe all the frequencies necessary to learn the unknown mechanical properties of the flexible body.

TABLE OF CONTENTS

ACKNOWLEDGMENTS	i
ABSTRACT	ii
LIST OF FIGURES	vii
LIST OF TABLES	viii
1 Introduction	1
NOMENCLATURE	1
2 Preliminaries	5
2.1 Vectors and Matrices	5
2.2 Transformation Matrices	5
2.3 Quaternions	6
3 Kinematics and Modeling	8
3.1 Kinematics	8
3.2 Positions	9
3.3 Velocities	10
3.4 Generalized Speeds and Partial Velocities	10
3.5 Accelerations	11
4 Equations of Motion	12
4.1 Applied Torques	12
4.2 Applied Forces	13
4.3 Simplified Representation of the Equations of Motion	14
4.4 Equations of motion in terms of the actuated states	14

5 Control Design	16
5.1 Control Law	16
5.2 Estimation of the Unknown Parameters	18
5.2.1 Building the ICL matrix	19
5.2.2 Self-Tuning Method for ICL	20
6 Stability Analysis	22
7 Flexible Spacecraft Maneuvers	26
7.1 Flexible appendage pointing to spacecraft relative velocity	26
7.1.1 Initial Conditions	26
7.1.2 Desired Trajectory	27
7.1.3 Controller Parameters	27
7.1.4 Simulation Results	28
7.2 Slew-Maneuvers	35
7.2.1 Desired Trajectory	35
7.2.2 Simulation Results	36
8 Discussion	41
9 Conclusions	43
REFERENCES	44
PUBLICATIONS	47
A Appendix	48
A.1 Partial velocity matrices	48

LIST OF FIGURES

Figure	Page
3.1 Spacecraft with a flexible appendage	8
3.2 Spacecraft with a flexible appendage modeled as n-links with torsional springs and dampers	8
7.1 Visual Representation of desired trajectory for scenario 1. The flexible ap- pendage is aligned with the velocity vector of the circular orbit around Earth, always facing normal to Earth.	28
7.2 Behavior of the tracking error represented as the mean of the attitude mis- match and spacecraft angular velocity error over a time span of 1200s. Both errors converge closer to zero as the number of links increases.	30
7.3 Behavior of the relative angular displacements of each link over a time-span of 1200s. The excitation phase of the update law emphasizes the initial os- cillations of the appendage as the number of links increases. However, once the estimates of the unknowns reach their true values, the frequency of the oscillations remains constant and the decaying rate of the waves is slower as n increases.	31
7.4 Behavior of the input commanded torques to the spacecraft hub over a time- span of 1200s. As the number of links increases, the behavior of the controller reflects the oscillations of the flexible appendage to maintain the desired atti- tude trajectory.	32

7.5	Behavior of the estimated spring coefficients compared to their actual values over a time-span of 1200s. The controller with ICL accurately estimates the unknown spring coefficients after the initial finite excitation that lasts about 20 seconds. For constant tuning parameter Γ for all three models, the excitation applied to the estimates of the unknown spring coefficients is less aggressive as the number of unknowns increases, but still sufficient to collect information for the learning matrix to drive the estimates to their true values.	33
7.6	Behavior of the estimated damping coefficients compared to their actual values over a time-span of 1200s. The controller with ICL accurately estimates the unknown damping coefficients after the initial finite excitation that lasts about 20 seconds. For constant tuning parameter Γ for all three models, the excitation applied to the estimates of the unknown damping coefficients does not show a significant difference as the number of unknowns increases.	34
7.7	Visual representation of the desired slew maneuvers performed every 200 seconds.	36
7.8	Mean error of the unknown parameters over a time-span of 1500s. The estimates of the unknowns accurately reach their true value for each maneuver as the magnitude of the mean error between actual and estimated values converges to 1×10^{-12} at the end of each maneuver.	37
7.9	Behavior of the tracking error for the second scenario represented by the attitude mismatch and spacecraft angular velocity error over a time span of 1500s. By the end of each maneuver, the mean of both errors for the controller with ICL converges closer to zero than the one of the non-adaptive controller.	38

7.10 Behavior of the relative angular displacements of each link for the second scenario over a time-span of 1500s. The oscillations of the flexible appendage controlled by a non-adaptive law have a higher decay rate than the ones controlled by the ICL-based adaptive law. However, a higher wave amplitude is observed for the first three maneuvers when the control law does not use the correct estimates of the unknown spring and damping coefficients. 39

7.11 Behavior of the input commanded torques on the spacecraft hub for the second scenario over a time-span of 1500s. For both cases of the second scenario, the x and y component of the torques do not differ, whereas the z component of the non-adaptive controller shows higher magnitude for the first three maneuvers which reflects the behavior of the flexible appendage. 40

LIST OF TABLES

Table	Page
7.1 Initial Attitude, Position, and Velocities of the Spacecraft Hub	27
7.2 Mass and dimensions of the spacecraft bodies	27
7.3 Control Gains Parameters	28
7.4 Relative percent error of the final unknown estimates for different number of links modeled	35
7.5 Initial estimates of the unknowns and their constant true values	35

1 Introduction

Dynamics and controls methods for flexible spacecraft were popular in the late 80s. However, with the advance in deployables technology and flexible materials, this topic has regained interest over the last decade. Moreover, as the demand for more complex and capable spacecraft increase, so does the complexity of controllers for maneuvering them. Flexible spacecraft experience a combination of different vibrational modes that may or may not exceed the controller's frequency bandwidth. When the former happens, the system generates undesired translational or rotational responses. Therefore, it is of high importance to define a high-fidelity model of these complex systems as well as a robust adaptive controller to address these challenges in flexible spacecraft. Classic dynamic models of a flexible spacecraft use a set of coupled equations between the rotational dynamics of the hub and the modal coordinates dynamics of the flexible appendage [1, 2]. When the flexible appendage acts as a cantilever beam, the Euler-Bernoulli beam assumption is employed to model it since it gives good approximations of the beam's dynamics for static loads [3]. For small displacements and known flexible properties, the method of assumed modes is generally a good approach because it provides an accurate analytical solution of the flexible dynamics [4]. However, several assumptions in these approaches like the exclusion of translational effects in the system and assumptions in the flexible behavior like its most important modes and mode shape functions could degrade the solution's accuracy when testing different sizes and properties of the flexible appendage. Analytical techniques like Lagrange's equation or Hamilton's equation exploit their energy-based nature to provide a solution to the equations of motion of this system, but are computationally slow, in particular when trigonometric functions are involved. Another approach that differs from the classical methods aforementioned is the one proposed by Kane and it is used for multi-body dynamics problems and referenced as Kane's method [5]. When comparing the performance of dynamic modeling between the classic analytical method: Lagrange's equation, and Kane's method, the latter provides a higher performance than the former in CPU time and number of operations for large mul-

multiple body systems [6, 7]. With this method, Lagrange multipliers and quasi-coordinates in the dynamics are avoided, the translational kinematics of the system are included, and the attitude parameters can be selected after the equations of motion are already derived. With Kane's equation, the generalized speeds of the system are defined, and the partial velocities of each body are solved with respect to each generalized speed. Therefore, with the idea that a finite amount of displacement sensors can be mounted on the flexible appendage, and feed their measurements back in the spacecraft's controller, the system is modeled as a hub connected to a n-series of rigid links connected by torsional springs and dampers. Its equations of motion are derived using Kane's equation given the multiple-bodies nature of the system, and the acting torques generated by the spacecraft and the joints' springs can be isolated for control and online estimation of the springs coefficients. Kane's equations can be efficiently represented in matrix form, which are easy to implement in a script and compute the equations of motion for any number of rigid bodies attached to each other [8].

One of the main challenges in the controller design of flexible spacecraft is the possibility of the spacecraft experiencing frequencies of modes that exceeds the controller's capabilities. If a complete sweep of the higher and lower frequencies of the flexible appendage is available for on-ground testing, the right controller can be designed and selected a priori. However, on-ground testing is limited in a sense that a full picture of the appendage's bandwidth is hard to obtain. For example, the Deployable Optical Telescope (DOT, 9-10) was only tested for small deformations at high frequency [9]. Moreover, results of the flexible behavior obtained from on-ground testing suffer from errors in mathematical modeling and more importantly could differ from permanent deformations that occur during storage and launch. For example, the Near-Earth Asteroid (NEA) Scout has four deployable booms to form a solar sail and it has been stored in the CubeSat deployer for several months before the mission's launch. Once deployed, the flexible behavior that was previously observed on-ground is not guaranteed to reflect the behavior the NEA Scout will experience during its mission due to the longevity of storage time.

To take into account of unknowns in a system's dynamics and improve the controller's robustness, the traditional approach is to treat the unknowns as a disturbance and compensate for it using a classic feedback controller. However, we are interested in accurately estimating unknowns in the dynamics to improve the controller's performance during the spacecraft's mission, and to save time and resources during on-ground testing. In this way, the controller can compensate unexpected uncertainties like failure in complete deployment or permanent deformations of the flexible appendage. One approach is to concurrently estimate the unknown variables in the dynamics using persistent excitation of the system, but persistently exciting a spacecraft is not ideal in a real-life scenario [10]. However, when state derivatives are observable and finite difference is not required in obtaining them, the persistent excitation required to estimate the unknowns can be replaced by a finite excitation [11]. To overcome the use of state derivatives, Integral Concurrent Learning (ICL) can be included to generate a finite excitation for online estimation [12]. With ICL, the dynamics is integrated over a small window of time and the available inputs and outputs measurements are used to build a learning matrix that is positive definite and guarantees convergence of the unknown parameters. Spacecraft maneuvering by employing ICL in the control scheme has already found application [13]. The control objective of this investigation is to track a desired trajectory, keeping physical quantities like the angle displacements and the angular velocities of the hub bounded. During the attitude tracking, the ICL collects information about the system's mechanics that are uncertain and uses it to provide a better estimation of the flexible appendage's mechanics.

The novelty of this investigation is to provide a more generalized framework for flexible spacecraft control design by exploiting Kane's method to include online parameters estimation using novel adaptive techniques. Furthermore, this research aims at minimizing resources employed in on-ground operations like limiting the amount of sensors mounted on a flexible appendage and its vibration analysis. The paper starts by introducing the mathematical development of the dynamics of the system using Kane's method and its kinematics

using quaternions as attitude parameters. Then, the controller design is presented, together with the implementation of integral concurrent learning in the adaptive law. The stability of the system is then proven using Lyapunov's theory and main results for two real-life applications for a CubeSat with a flexible appendage are reported.

2 Preliminaries

In this section, some preliminaries on the conventions and notations used throughout this paper for vector and matrix representations, transformation matrices, quaternions and their related operations are listed.

2.1 Vectors and Matrices

Vectors will be expressed in bold italic letters as $\mathbf{x} \in \mathbb{R}^n$. The i th component of the vector \mathbf{x} will be expressed as x_i . To describe the coordinate system a vector is expressed in, a superscript capital letter will precede the vector. For example, the vector ${}^N\mathbf{x}$ is expressed in the N coordinate system and the vector ${}^B\mathbf{x}$ is expressed in the B coordinate system.

The cross product between two vectors can be represented as $\mathbf{x} \times \mathbf{y} = \mathbf{x}^\times \mathbf{y} = -\mathbf{y}^\times \mathbf{x}$, where the superscript \times on a vector $\mathbf{x} \in \mathbb{R}^3$ represents its skew-symmetric matrix:

$$\mathbf{x}^\times \triangleq \begin{bmatrix} 0 & -x_3 & x_2 \\ x_3 & 0 & -x_1 \\ -x_2 & x_1 & 0 \end{bmatrix} \quad (2.1)$$

The operator $B = \text{blkdiag}(A_1, \dots, A_n) \in \mathbb{R}^{nm \times nm}$ with $A \in \mathbb{R}^{m \times m}$ is read as:

$$B = \text{blkdiag}(A_1, \dots, A_n) = \begin{bmatrix} A_1 & 0 & 0 \\ 0 & \ddots & 0 \\ 0 & 0 & A_n \end{bmatrix} \quad (2.2)$$

2.2 Transformation Matrices

General matrices will be expressed in capitalized italic letter as $A \in \mathbb{R}^{m \times n}$. Transformation matrices are matrices that translate one vector from one coordinate system to another. Commonly, in analytical dynamics, the term rotation matrix refers to the matrix that converts a vector from an inertial coordinate system to the body-fixed coordinate system, and the term direction-cosine matrix represents the transformation from body-fixed coordinate

system to the inertial one. To avoid confusion, the following notation is used for general rotations from coordinate system A to coordinate system B : $R^{A \rightarrow B}$. Successive rotations are obtained as:

$$R^{A \rightarrow C} = R^{B \rightarrow C} \cdot R^{A \rightarrow B} \quad (2.3)$$

2.3 Quaternions

A quaternion is a set of parameters composed of a scalar term $q_w \in \mathbb{R}$ and a vectorial part $\mathbf{q}_v \in \mathbb{R}^3$. For attitude representation, the unit quaternion is used, meaning the norm between the scalar and vectorial part is equal to 1 because of the constraint imposed to bring the representation to three degrees of freedom (DoF). In this paper, the quaternion order has the vectorial part first and scalar term last. Then, a quaternion is $\mathbf{q} = \begin{bmatrix} \mathbf{q}_v^T & q_w \end{bmatrix}^T \in \mathbb{R}^4$ with the following constraint:

$$q_w = \sqrt{1 - \mathbf{q}_v^T \mathbf{q}_v} \quad (2.4)$$

The addition between two quaternions \mathbf{q} and \mathbf{p} follows the same vector algebra, whereas the product between two quaternion is defined using \otimes and is calculated as follows:

$$\mathbf{q} \otimes \mathbf{p} = \begin{bmatrix} q_w \mathbf{p}_v + p_w \mathbf{q}_v + \mathbf{q}_v^\times \mathbf{p}_v \\ q_w p_w - \mathbf{q}_v^T \mathbf{p}_v \end{bmatrix} \quad (2.5)$$

Throughout this paper, quaternions represent the attitude of a rigid body expressed in the inertial coordinate system; therefore, it can be used to derive the transformation matrix from a body-fixed coordinate system to the inertial one as follows:

$$R^{B \rightarrow N} = \left([{}^N q_w]^2 - [{}^N \mathbf{q}_v]^T [{}^N \mathbf{q}_v] \right) I_3 + 2 [{}^N \mathbf{q}_v] [{}^N \mathbf{q}_v]^T - 2 [{}^N q_w] [{}^N \mathbf{q}_v]^\times \quad (2.6)$$

Furthermore, the quaternion of a rotating rigid body follows the following kinematic law:

$${}^N \dot{\mathbf{q}} = \frac{1}{2} \begin{bmatrix} {}^B \boldsymbol{\omega}_B \\ 0 \end{bmatrix} \otimes {}^N \mathbf{q} = \frac{1}{2} {}^N \mathbf{q} \otimes \begin{bmatrix} {}^N \boldsymbol{\omega}_B \\ 0 \end{bmatrix} \quad (2.7)$$

where ${}^N\boldsymbol{\omega}_B \in \mathbb{R}^3$ is the rotation of the coordinate system B with respect to N , expressed in the N coordinate system.

3 Kinematics and Modeling

3.1 Kinematics

Consider a flexible appendage attached to the spacecraft hub as shown in Figure 3.1. To provide a high-fidelity model of the flexible appendage, we design it as a series of n -links connected by torsional springs and dampers as shown in Figure 3.2. The spacecraft hub has mass m_h , height H in the \hat{b}_z component, length L in the \hat{b}_x component, and width W in the \hat{b}_y component. Each link has length l_y defined in the y component of the body and mass m_l , and it has a rectangular cross-sectional area of $l_x \times l_z$. Furthermore, each joint has torsional spring coefficient of k_s and damping coefficient of c_s . It is assumed the flexible appendage has one degree of freedom about the body z axis, but a general formulation is provided.

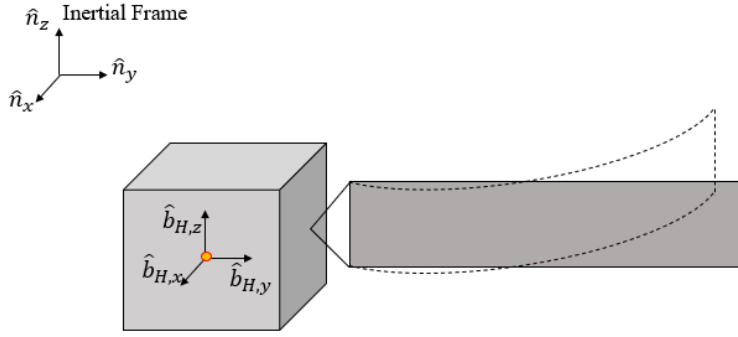


Figure 3.1 Spacecraft with a flexible appendage

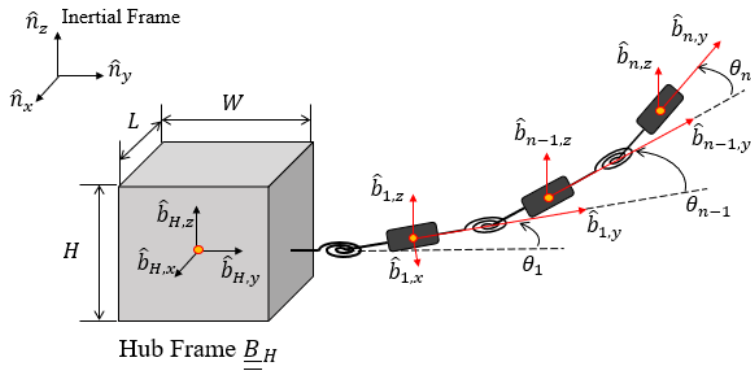


Figure 3.2 Spacecraft with a flexible appendage modeled as n -links with torsional springs and dampers

The spring coefficients of each joint of the flexible appendage can be determined by analyzing each link and equating the bending moment due to the deflection by a tip load

to the spring moment at that joint [14]. It is important to note that these coefficients are only calculated with this approach to run the simulation of the dynamics of the system and evaluate the performance of the update law. In reality, the controller will best estimate the true values of these coefficients. The spring coefficients at each joint are evaluated as:

$$k_i = \frac{EI_y}{l_{link}} \quad (3.1)$$

where E is the Young's modulus, I_y is the moment of inertia about the cross-sectional area of the link, l_{link} is the length of the link, and $i = 2 : n$ with n being the number of links modeled. The joint that attaches the flexible appendage to the hub is the joint of the deployment mechanism, which by design is known, but is also treated as uncertain parameter because of potential deformations during storage or failure in deployment. The damping coefficient at each joint is evaluated as:

$$c_i = 2\zeta_i\sqrt{m_L k_i} \quad (3.2)$$

where m_L is the mass of the link and ζ_i is the damping ratio, for $i = 1 : n$.

3.2 Positions

The position vectors of each body are determined as:

$${}^N \mathbf{r}_H = {}^N \mathbf{r}_H \quad (3.3)$$

$${}^N \mathbf{r}_{L1} = {}^N \mathbf{r}_H + {}^N \mathbf{r}_{H \rightarrow j1} - {}^N \mathbf{r}_{L1 \rightarrow j1} \quad (3.4)$$

$${}^N \mathbf{r}_{Li} = {}^N \mathbf{r}_{Li-1} + {}^N \mathbf{r}_{Li-1 \rightarrow ji} - {}^N \mathbf{r}_{Li \rightarrow ji} \quad (3.5)$$

where ${}^N \mathbf{r}_{Li \rightarrow ji}$ is the path vector going from the center of mass of the link i to joint i and obtained as:

$${}^N \mathbf{r}_{Li \rightarrow ji} = \frac{1}{2} R^{Li \rightarrow N} \begin{bmatrix} 0 & l_{link} & 0 \end{bmatrix}^T \quad (3.6)$$

with l_{link} being the length of the link.

3.3 Velocities

The inertial angular velocity of each body expressed in its body-fixed frame is obtained as:

$${}^H\boldsymbol{\omega}_H = {}^H\boldsymbol{\omega}_H \quad (3.7)$$

$${}^{Li}\boldsymbol{\omega}_{Li} = R^{H \rightarrow Li} {}^H\boldsymbol{\omega}_H + \sum_{k=1}^i R^{Lk \rightarrow Li} \Psi \dot{\boldsymbol{\theta}}_k \quad (3.8)$$

where ${}^H\boldsymbol{\omega}_H$ is the angular velocity vector of the hub expressed in the body-fixed frame, Ψ is the partial joint matrix that defines the degrees of freedom of the joint for which its derivation can be seen from Reference [8], and $\dot{\boldsymbol{\theta}}_i$ is the angular displacement rate of the i th link relative to the previous one. The inertial linear velocity of each body expressed in the inertial frame is obtained after taking the first time derivative of the position vectors and using the transport theorem because of the different rotations each body experiences.

$${}^N\mathbf{v}_H = v_H \quad (3.9)$$

$${}^N\mathbf{v}_{L1} = {}^N\mathbf{v}_H + (R^{H \rightarrow NH}\boldsymbol{\omega}_H)^\times {}^N\mathbf{r}_{H \rightarrow j1} - (R^{L1 \rightarrow NL1}\boldsymbol{\omega}_{L1})^\times {}^N\mathbf{r}_{L1 \rightarrow j1} \quad (3.10)$$

$$\begin{aligned} {}^N\mathbf{v}_{Li} = & {}^N\mathbf{v}_{Li-1} + (R^{Li-1 \rightarrow NLi-1}\boldsymbol{\omega}_{Li-1})^\times {}^N\mathbf{r}_{Li-1 \rightarrow ji} + \\ & - (R^{Li \rightarrow NLi}\boldsymbol{\omega}_{Li})^\times {}^N\mathbf{r}_{Li \rightarrow ji} \end{aligned} \quad (3.11)$$

3.4 Generalized Speeds and Partial Velocities

Kane's equation introduces the concept of generalized speeds and partial velocities to derive the equations of motion of the system. Let the generalized speeds vector of the system be:

$$\mathbf{u} = \left[{}^H\boldsymbol{\omega}_H^T \quad \dot{\theta}_1 \quad \dots \quad \dot{\theta}_n \quad {}^N\mathbf{v}_H^T \right]^T \in \mathbb{R}^{6+n} \quad (3.12)$$

where, ${}^H\boldsymbol{\omega}_H$ is the angular velocity components of the hub in its frame, $\dot{\theta}_{1:n}$ are the angular rate displacements of each link with respect to one another with n being the number of links

modeled, and ${}^N\mathbf{v}_H$ is the linear velocity of the hub expressed in the inertial frame. Thus, both the velocities of each body are rewritten as a function of the partial velocities and generalized speeds. If we collect the velocities of each body into vectors, we obtain:

$$\mathbf{v} = \begin{bmatrix} {}^N\mathbf{v}_H^T & {}^N\mathbf{v}_{L1}^T & \dots & {}^N\mathbf{v}_{Ln}^T \end{bmatrix}^T = V\mathbf{u} \quad (3.13)$$

$$\boldsymbol{\omega} = \begin{bmatrix} {}^H\boldsymbol{\omega}_H^T & {}^{L1}\boldsymbol{\omega}_{L1}^T & \dots & {}^{Ln}\boldsymbol{\omega}_{Ln}^T \end{bmatrix}^T = \Omega\mathbf{u} \quad (3.14)$$

where $\Omega \in \mathbb{R}^{q \times m}$ is the angular partial velocity matrix defined in (A.1) and $V \in \mathbb{R}^{q \times m}$ is the linear partial velocity matrix defined in (A.2), with $q = 3 + 3n$ and $m = 6 + n$.

3.5 Accelerations

From this parametrization, we can derive the linear accelerations \mathbf{a} and the angular accelerations $\boldsymbol{\alpha}$ of each body as:

$$\mathbf{a} = V\dot{\mathbf{u}} + \dot{V}\mathbf{u} \quad (3.15)$$

$$\boldsymbol{\alpha} = \Omega\dot{\mathbf{u}} + \dot{\Omega}\mathbf{u} \quad (3.16)$$

The decomposition of the accelerations in Equation (3.15) and (3.16) will be exploited in the derivation of the equations of motion as it allows writing them as a first order differential equation with respect to the generalized speeds \mathbf{u} [8].

4 Equations of Motion

The equations of motion are determined using Kane's equation in matrix form as:

$$V^T \mathbf{F} + \Omega^T \mathbf{T} = V^T M \mathbf{a} + \Omega^T (J \boldsymbol{\alpha} + \{\boldsymbol{\omega}\}^\times J \boldsymbol{\omega}) \quad (4.1)$$

where $\mathbf{F} \in \mathbb{R}^q$ and $\mathbf{T} \in \mathbb{R}^q$ are respectively the forces and torques applied on each body, $J = \text{blkdiag}(J_H, J_{L1}, \dots, J_{Ln}) \in \mathbb{R}^{q \times q}$, $M = \text{blkdiag}(m_H I_3, m_{L1} I_3, \dots, m_{Ln} I_3) \in \mathbb{R}^{q \times q}$, and $\{\boldsymbol{\omega}\}^\times \triangleq \text{blkdiag}({}^H \boldsymbol{\omega}_H^\times, {}^{L1} \boldsymbol{\omega}_{L1}^\times, \dots, {}^{Ln} \boldsymbol{\omega}_{Ln}^\times) \in \mathbb{R}^{q \times q}$, with blkdiag defined in Equation (2.2) and $q = 3 + 3n$. Substituting Equation (3.15) and (3.16) in Equation (4.1), a first-order differential equation is obtained:

$$(V^T M V + \Omega^T J \Omega) \dot{\mathbf{u}} = V^T \mathbf{F} + \Omega^T \mathbf{T} - \left(\Omega^T J \dot{\Omega} + \Omega^T \{\boldsymbol{\omega}\}^\times J \Omega + V^T M \dot{V} \right) \mathbf{u} \quad (4.2)$$

In Kane's equation, only the forces and torques directly applied to each individual body are included thanks to the use of partial velocities, which map the contribution of all the forces and torques to a specific body.

4.1 Applied Torques

The torques applied to the spacecraft hub are the ones generated by the controller $\boldsymbol{\tau}_k \in \mathbb{R}^3$ and the first joint, whereas the ones applied on each link are the net torques generated by its two end joints. The torque generated by the i th joint is:

$$\boldsymbol{\tau}_{ji} = k_i \Psi \theta_i + c_i \Psi \dot{\theta}_i \quad (4.3)$$

where k_i and c_i are the spring and damping coefficients, respectively, θ_i is the relative angular displacement of the i th link with respect to the previous one and $\dot{\theta}_i$ its time derivative.

The vector form of the applied torques is then:

$$\mathbf{T} = \left[(\boldsymbol{\tau}_k - \boldsymbol{\tau}_{j1})^T \quad (\boldsymbol{\tau}_{j1} - \boldsymbol{\tau}_{j2})^T \quad \cdots \quad (\boldsymbol{\tau}_{jn-1} - \boldsymbol{\tau}_{jn})^T \quad \boldsymbol{\tau}_{jn}^T \right]^T \quad (4.4)$$

The control torques are then isolated from the joints' torques as:

$$\mathbf{T} = \boldsymbol{\tau}_c + \boldsymbol{\tau}_j \quad (4.5)$$

where $\boldsymbol{\tau}_c$ is: $\begin{bmatrix} \boldsymbol{\tau}_k^T & 0_{1 \times 3n} \end{bmatrix}^T$ with n , again, being the number of links modeled. Furthermore, the product $\Omega^T \boldsymbol{\tau}_c$ is equal to $\boldsymbol{\tau}_c$ because the first 3×3 block of Ω^T is the identity matrix, and its other columns are multiplied by zeros.

Since the objective of this paper is to estimate the parameters of the flexible dynamics like the spring and damping coefficients of each joint, a vector of constant unknowns Θ is defined:

$$\Theta \triangleq \begin{bmatrix} k_{j1} & \cdots & k_{jn} & c_{j1} & \cdots & c_{jn} \end{bmatrix}^T \quad (4.6)$$

Then, a linear regression matrix Y allows the joints torque to be linearly parametrized as:

$$\Omega^T \boldsymbol{\tau}_j = Y \Theta \quad (4.7)$$

with:

$$Y = \Omega^T \begin{bmatrix} \Psi\theta_1 & 0 & 0 & 0 & \Psi\dot{\theta}_1 & 0 & 0 & 0 \\ -\Psi\theta_1 & \Psi\theta_2 & 0 & 0 & -\Psi\dot{\theta}_1 & \Psi\dot{\theta}_2 & 0 & 0 \\ 0 & \ddots & \ddots & 0 & 0 & \ddots & \ddots & 0 \\ 0 & 0 & -\Psi\theta_{n-1} & \Psi\theta_n & 0 & 0 & -\Psi\dot{\theta}_{n-1} & \Psi\dot{\theta}_n \\ 0 & 0 & 0 & -\Psi\theta_n & 0 & 0 & 0 & -\Psi\dot{\theta}_n \end{bmatrix} \quad (4.8)$$

4.2 Applied Forces

Since the springs and dampers at each joint exert pure torques, they do not apply forces on any of the bodies of the system. Thus, we only consider any external forces applied on the center of mass of each body, which could be gravitational, drag, and/or thruster forces.

Based on the system design and working scenarios, the force vector \mathbf{F} is built and in general terms takes the form: $\mathbf{F} = \begin{bmatrix} \mathbf{F}_H^T & \mathbf{F}_{L1}^T & \cdots & \mathbf{F}_{Ln}^T \end{bmatrix}^T$ where \mathbf{F}_i is the force applied on the i th

body.

4.3 Simplified Representation of the Equations of Motion

For further simplification of the upcoming control design, the following terms are defined:

$$W \triangleq V^T M V + \Omega^T J \Omega \quad (4.9)$$

$$\mathbf{N} \triangleq V^T \mathbf{F} - \left(\Omega^T J \dot{\Omega} + \Omega^T \{\boldsymbol{\omega}\}^\times J \Omega + V^T M \dot{V} \right) \mathbf{u} \quad (4.10)$$

The equations of motion for the system then become:

$$W \dot{\mathbf{u}} = \mathbf{N} + Y \boldsymbol{\Theta} + \boldsymbol{\tau}_c \quad (4.11)$$

and they can be numerically solved using LDL Cholesky decomposition by exploiting the symmetry of W .

4.4 Equations of motion in terms of the actuated states

As previously mentioned, the controller only applies torques on the spacecraft hub, and the control objective is to track the angular velocity of the hub and its attitude. The system is underactuated because there are more states than actuated ones. Then, Equation (4.11) is rewritten as a function of the actuated states only using a rearrangement of the equations of motion [15].

The actuated states are $\mathbf{u}_a = {}^H \boldsymbol{\omega}_H$ and the underactuated states are $\mathbf{u}_u = [\dot{\theta}_1, \dots, \dot{\theta}_n, {}^N \mathbf{v}_H]^T$. Thus, the equation of motion is now rewritten by generating blocks within the matrices in Equation (4.11) as:

$$\begin{bmatrix} W_{aa} & W_{au} \\ W_{ua} & W_{uu} \end{bmatrix} \begin{bmatrix} {}^H \dot{\boldsymbol{\omega}}_H \\ \dot{\mathbf{u}}_u \end{bmatrix} = \begin{bmatrix} \mathbf{N}_a \\ \mathbf{N}_u \end{bmatrix} + \begin{bmatrix} Y_a \\ Y_u \end{bmatrix} \boldsymbol{\Theta} + \begin{bmatrix} \boldsymbol{\tau}_k \\ 0 \end{bmatrix} \quad (4.12)$$

With some manipulation, the equation can be rewritten to be solved for only ${}^H\dot{\boldsymbol{\omega}}_H$ as:

$$W_d {}^H\dot{\boldsymbol{\omega}}_H = \mathbf{N}_d + Y_d \boldsymbol{\Theta} + \boldsymbol{\tau}_k \quad (4.13)$$

where:

$$W_d \triangleq W_{aa} - W_{au} W_{uu}^{-1} W_{ua} \quad (4.14)$$

$$\mathbf{N}_d \triangleq \mathbf{N}_a - W_{au} W_{uu}^{-1} \mathbf{N}_u \quad (4.15)$$

$$Y_d \triangleq Y_a - W_{au} W_{uu}^{-1} Y_u \quad (4.16)$$

and the underactuated dynamics is:

$$W_{uu} \dot{\mathbf{u}}_u = \mathbf{N}_u + Y_u \boldsymbol{\Theta} - W_{ua} {}^H\dot{\boldsymbol{\omega}}_H \quad (4.17)$$

5 Control Design

The control objective is to have a flexible spacecraft of partially unknown dynamics track a desired trajectory while estimating the unknowns.

5.1 Control Law

The desired trajectory is made of a desired attitude trajectory and desired angular velocity of the spacecraft hub. Therefore, an auxiliary error state is introduced and used to design the controller. The error state is defined as:

$$\mathbf{r}(t) = {}^H\tilde{\boldsymbol{\omega}}(t) + \alpha\tilde{\mathbf{q}}_v(t) \quad (5.1)$$

where ${}^H\tilde{\boldsymbol{\omega}}(t)$ is the difference between the angular velocity of the hub at time t with the desired angular velocity at that same time, α is a positive scalar control gain, and $\tilde{\mathbf{q}}_v(t)$ is the vector part of the quaternion error between the body-fixed frame H and the desired reference frame D .

Since the desired angular velocity is represented in the desired reference frame D , it needs to be expressed in the body-fixed frame H . Therefore,

$${}^H\tilde{\boldsymbol{\omega}}(t) = {}^H\boldsymbol{\omega}_H(t) - R(t)^{D \rightarrow H} {}^D\boldsymbol{\omega}_{des}(t) \quad (5.2)$$

The transformation matrix $R(t)^{D \rightarrow H}$ is obtained as successive rotations using:

$$R(t)^{D \rightarrow H} = R(t)^{N \rightarrow H} \cdot R(t)^{D \rightarrow N} = [R(t)^{H \rightarrow N}]^T \cdot R(t)^{D \rightarrow N} \quad (5.3)$$

The transformation matrices $R(t)^{H \rightarrow N}$ and $R(t)^{D \rightarrow N}$ are obtained with Equation (2.6) using ${}^H\boldsymbol{\omega}_H(t)$ and ${}^D\boldsymbol{\omega}_{des}(t)$ respectively. The quaternion error $\tilde{\mathbf{q}}(t)$ is obtained with the quaternion kinematic law in Equation (2.7), which results in the vectorial and scalar parts of the

quaternion error to be obtained as:

$$\dot{\tilde{\mathbf{q}}}_v(t) = \frac{1}{2} \left(\tilde{\mathbf{q}}_v^\times(t) + \tilde{q}_w(t) I_3 \right) {}^H \tilde{\boldsymbol{\omega}}(t) \quad (5.4)$$

$$\dot{\tilde{q}}_w(t) = -\frac{1}{2} \tilde{\mathbf{q}}_v^T {}^H \tilde{\boldsymbol{\omega}}(t) \quad (5.5)$$

using ${}^H \tilde{\boldsymbol{\omega}}(t)$ instead of ${}^B \boldsymbol{\omega}$. At any time t , the quaternion error can also be computed using the quaternion product between the inverse of the desired quaternion $\mathbf{q}_{des}(t)$ and the spacecraft quaternion $\mathbf{q}(t)$ as:

$$\tilde{\mathbf{q}}(t) = \mathbf{q}_{des}^{-1}(t) \otimes \mathbf{q}(t) \quad (5.6)$$

The open-loop error dynamics is obtained by taking the first-time derivative of Equation (5.1) and substituting the dynamics from Equation (4.13), resulting in:

$$\dot{\mathbf{r}}(t) = W_d^{-1}(t) (\mathbf{N}_d(t) + Y_d(t) \boldsymbol{\Theta} + \boldsymbol{\tau}_k(t)) + \boldsymbol{\tau}_{track}(t) \quad (5.7)$$

with $\boldsymbol{\tau}_{track}(t) \triangleq -\dot{R}(t)^{D \rightarrow H} {}^D \boldsymbol{\omega}_{des}(t) - R(t)^{D \rightarrow H} {}^D \dot{\boldsymbol{\omega}}_{des}(t) + \alpha \dot{\tilde{\mathbf{q}}}_v(t)$.

For the nonlinear system of equations with unknown dynamics, the following Lyapunov-based controller is proposed:

$$\boldsymbol{\tau}_k(t) = -\mathbf{N}_d(t) - Y_d(t) \hat{\boldsymbol{\Theta}}(t) - W_d(t) \boldsymbol{\tau}_{track}(t) - W_d(t) P^{-1} (\kappa \mathbf{r}(t) + \beta \tilde{\mathbf{q}}_v(t)) \quad (5.8)$$

where $\hat{\boldsymbol{\Theta}}(t)$ is the estimate of the unknowns $\boldsymbol{\Theta}$ at time t , κ and β are positive scalar control gains, and P is a positive definite Lyapunov matrix which will be selected in the stability analysis. The error between the actual unknowns and their estimate at time t is defined as: $\tilde{\boldsymbol{\Theta}}(t) = \boldsymbol{\Theta} - \hat{\boldsymbol{\Theta}}(t)$. Then, the closed-loop dynamics is obtained by substituting Equation (5.8) in (5.7), resulting in:

$$\dot{\mathbf{r}}(t) = W_d^{-1}(t) Y_d(t) \tilde{\boldsymbol{\Theta}}(t) - W_d(t) P^{-1} (\kappa \mathbf{r}(t) + \beta \tilde{\mathbf{q}}_v(t)) \quad (5.9)$$

5.2 Estimation of the Unknown Parameters

The control law in (5.8) uses the current estimates of the unknown parameters to drive the system to a desired trajectory. Therefore, an update law for the estimates must be designed. For these types of problems, the most common approach is to treat the unknowns as a disturbance and update the estimates of the unknowns with a linear feedback law to compensate for them and drive the spacecraft attitude error to zero. However, this investigation aims to accurately learn the unknown parameters to improve the performance of the controller for specific maneuvers. If the flexible appendage has a payload like a camera or is a deployable flexible panel for which its motion must be precisely controlled, having a high-fidelity model of the flexible dynamics is required. If the system is subject to persistent excitation (PE), the estimates of the unknown will accurately converge to their true value [10]. However, PE is hard to check onboard and undesirable for real-life applications. Instead, a finite excitation (FE) can be employed to make the update law more realistic in a sense that it finds applications to real-life scenarios, and a basis function for the unknown error can be derived from the dynamics. The work from Reference [11] shows that this basis function can be obtained from the equations of motion when the first-time derivative of the states are available for measurement and not estimated. Again, this approach has assumptions that do not hold in real-life applications since time derivatives of the states are most likely not available, and using differentiation techniques have several drawbacks like numerical errors, singularities, and inaccuracies that depend on the capabilities of the onboard computer.

However, if the dynamics is integrated over a small window of time after a FE is applied to the system, the resulting integrals of the applied inputs and output states can be collected over time to build a positive definite learning matrix [12]. This approach is referred as integral concurrent learning (ICL) and offers a solution for estimating unknowns that can be linearly parametrized and are function of known variables like inputs and states. For the purpose of this investigation, the states are assumed to be perfectly measurable and noise-free.

Then, the update law for this system becomes:

$$\dot{\tilde{\Theta}}(t) = \text{proj} \left(\Gamma [PW_d^{-1}(t)Y_d(t)]^T \mathbf{r}(t) + \Gamma \Lambda \left(\sum_{i=1}^N \mathcal{Y}_i^T \mathcal{Y}_i \right) \tilde{\Theta}(t) \right) \quad (5.10)$$

where Γ and Λ are positive definite control gain matrices, $\left(\sum_{i=1}^N \mathcal{Y}_i^T \mathcal{Y}_i \right)$ is a positive definite learning matrix obtained using ICL. A projector operator $\text{proj}(\cdot)$ is introduced in the adaptive law to bound the estimates to physically meaningful values. Details on building the learning matrix and guaranteeing its positive-definiteness follow.

5.2.1 Building the ICL matrix

Reconsider the system in Equation (4.11) and integrate over a small window of time Δt :

$$\dot{\mathbf{u}}(t) = W^{-1}(t) (\mathbf{N}(t) + Y(t)\Theta + \boldsymbol{\tau}_c(t)) \quad (5.11)$$

$$\mathbf{u}(t_i) - \mathbf{u}(t_i - \Delta t) = \int_{t_i - \Delta t}^{t_i} W^{-1}(t) (\mathbf{N}(t) + Y(t)\Theta + \boldsymbol{\tau}_c(t)) dt \quad (5.12)$$

We now define the following integrals:

$$\mathcal{Y}_i = \mathcal{Y}(t_i) \triangleq \int_{t_i - \Delta t}^{t_i} W^{-1}(t) Y(t) dt \quad (5.13)$$

$$\mathbf{u}_i = \mathbf{u}(t_i) \triangleq \mathbf{u}(t_i) - \mathbf{u}(t_i - \Delta t) - \int_{t_i - \Delta t}^{t_i} W^{-1}(t) (\mathbf{N}(t) + \boldsymbol{\tau}_c(t)) dt \quad (5.14)$$

So that, Equation (5.11) becomes:

$$\mathbf{u}(t_i) = \mathcal{Y}(t_i)\Theta \quad (5.15)$$

The integral terms \mathcal{Y}_i and \mathbf{u}_i are collected until the sum $\sum_{i=1}^N \mathcal{Y}_i^T \mathcal{Y}_i$ is positive definite. This condition is met when:

$$\lambda_{\min} \left(\sum_{i=1}^N \mathcal{Y}_i^T \mathcal{Y}_i \right) \geq \bar{\lambda} \quad (5.16)$$

where $\bar{\lambda}$ is a positive scalar used as threshold for the finite excitation, and N is the number of data points stored. The collection of the ICL terms \mathcal{Y}_i and \mathbf{u}_i is optimized using a singular value decomposition algorithm [16] which discards repeating or very similar data points and only implements the ones that would enrich the learning matrix by maximizing its singular values. The integrals in Equation (5.13) and (5.14) are obtained using the Riemann Sum in order to reduce the propagation of numerical errors.

5.2.2 Self-Tuning Method for ICL

One of the novelties of this paper is the introduction of the concept of self-tuning for the learning matrix. As the number of links modeled increases, so does the number of observable modes of the flexible appendage, and more information about the mode shapes experienced by the flexible body is collected. This leads to the resulting ICL matrix having convergence rates or eigenvalues associated with each unknown of different orders of magnitude because more information is being added in the learning matrix until the condition of minimum eigenvalue in Equation (5.16) is met. Eigenvalues of different orders of magnitude result in a much faster convergence for some unknowns compared to others; therefore, the projector operator in Equation (5.10) will prevent the fast estimates to update since they would exceed the operator bounds. The solution to this problem proposed in this paper is to tune the control gain matrix Λ such that the product $\Lambda \sum_{i=1}^N \mathcal{Y}_i^T \mathcal{Y}_i$ has a desired spectrum of eigenvalues. This is accomplished by exploiting the positive definiteness of $\sum_{i=1}^N \mathcal{Y}_i^T \mathcal{Y}_i$, meaning that it is not singular and its inverse exists. The matrix is decomposed using a singular value decomposition (SVD):

$$\sum_{i=1}^N \mathcal{Y}_i^T \mathcal{Y}_i = U \Sigma L^T \quad (5.17)$$

Then, a matrix that conserves the same coupling of the ICL matrix but has different eigenvalues is designed as $K_{ICL} = U \Sigma_{des} L^T$, and the control gain matrix Λ is designed as:

$$\Lambda = K_{ICL} \left[\sum_{i=1}^N \mathcal{Y}_i^T \mathcal{Y}_i \right]^{-1} \quad (5.18)$$

The control gain matrix Λ can only be determined when $\left[\sum_{i=1}^N \mathcal{Y}_i^T \mathcal{Y}_i\right]^{-1}$ exists, so it is switched in the adaptive law as:

$$\Lambda = \begin{cases} 0 & 0 \leq t \leq t_\lambda \\ K_{ICL} \left[\sum_{i=1}^N \mathcal{Y}_i^T \mathcal{Y}_i\right]^{-1} & t_\lambda \leq t < \infty \end{cases} \quad (5.19)$$

where t_λ is the time when the condition in Equation (5.16) is met and implies $\det\left(\sum_{i=1}^N \mathcal{Y}_i^T \mathcal{Y}_i\right) \neq 0$.

From this development, two adaptive laws are obtained: Equation (5.10) is the one used for proof of stability, and one for controller implementation is obtained by combining the relationship found in Equation (5.15) and (5.10), leading to:

$$\dot{\hat{\Theta}}(t) = \text{proj} \left(\Gamma \left[PW_d^{-1}(t) Y_d(t) \right]^T \mathbf{r}(t) + \Gamma \Lambda \sum_{i=1}^N \mathcal{Y}_i^T \left(\mathbf{u}_i - \mathcal{Y}_i \hat{\Theta}(t) \right) \right) \quad (5.20)$$

6 Stability Analysis

Two theorems are formulated to show the stability of the system's response during and after the finite excitation stage. The first theorem is used to show boundedness of the unknowns and convergence of the tracking error during the excitation applied to enrich the learning matrix, whereas the second theorem is employed to show the error of the unknowns is driven to zero with the ICL matrix after the excitation has been applied.

Theorem 1. *Consider the system described in Equation (4.13) with attitude dynamics described by Equation (2.7). Then the control law designed in Equation (5.8) and update law designed in Equation (5.10) guarantee global asymptotic stability for the attitude tracking error $\tilde{\mathbf{q}}_v$ and the spacecraft's angular velocity tracking error $\tilde{\boldsymbol{\omega}}$ in a sense that $\lim_{t \rightarrow \infty} \begin{bmatrix} \tilde{\boldsymbol{\omega}} & \tilde{\mathbf{q}}_v \end{bmatrix} = 0$ and boundedness of the unknowns error $\tilde{\boldsymbol{\Theta}}$ for any $0 \leq t < t_\lambda$.*

Proof. Consider the extended state $\boldsymbol{\eta} = \begin{bmatrix} \tilde{\boldsymbol{\omega}}^T & \tilde{\mathbf{q}}_v^T & \tilde{\boldsymbol{\Theta}}^T \end{bmatrix}^T \in \mathbb{R}^{6+p}$ with p being the number of unknowns, and let $V(\boldsymbol{\eta})$ be a positive definite Lyapunov's function defined as:

$$V(\boldsymbol{\eta}) = \frac{1}{2} \mathbf{r}^T P \mathbf{r} + \frac{1}{2} \tilde{\boldsymbol{\Theta}}^T \Gamma^{-1} \tilde{\boldsymbol{\Theta}} + \beta [\tilde{\mathbf{q}}_v^T \tilde{\mathbf{q}}_v + (\tilde{\mathbf{q}}_w - 1)^2] \quad (6.1)$$

and bounded by:

$$\gamma_1 \|\boldsymbol{\eta}\|^2 \leq V(\boldsymbol{\eta}) \leq \gamma_2 \|\boldsymbol{\eta}\|^2 \quad (6.2)$$

where γ_1 and γ_2 are positive bounding scalars.

Substituting Equation (5.4), (5.5), (5.7), (5.8), and (5.10) in the first-time derivative of Equation (6.1) leads to:

$$\dot{V}(\boldsymbol{\eta}) = -\mathbf{r}^T (\kappa \tilde{\mathbf{r}} + \beta \tilde{\mathbf{q}}_v) + \beta \tilde{\mathbf{q}}_v^T \tilde{\boldsymbol{\omega}} \quad (6.3)$$

Since Equation (6.3) is not enough to show stability of the attitude mismatch and angular velocity error, the tracking signal \mathbf{r} is expanded in Equation (6.3) using (5.1), which yields:

$$\dot{V}(\boldsymbol{\eta}) = -\tilde{\boldsymbol{\omega}}^T \kappa \tilde{\boldsymbol{\omega}} - \tilde{\mathbf{q}}_v^T (\alpha \beta + \alpha^2 \kappa) \tilde{\mathbf{q}}_v - 2\kappa \alpha \tilde{\boldsymbol{\omega}}^T \tilde{\mathbf{q}}_v \quad (6.4)$$

Further, Equation (6.4) can be upper-bounded using Hölder's inequality: $\|x^T y\| \leq \|x\| \|y\|$ as:

$$\dot{V}(\boldsymbol{\eta}) \leq -\kappa \|\tilde{\boldsymbol{\omega}}\|^2 - \lambda_q \|\tilde{\mathbf{q}}_v\|^2 - 2\kappa\alpha \|\tilde{\boldsymbol{\omega}}\| \cdot \|\tilde{\mathbf{q}}_v\| \quad (6.5)$$

with λ_q equal to $(\alpha\beta + \alpha^2\kappa)$. Equation (6.5) can then be manipulated as:

$$\dot{V}(\boldsymbol{\eta}) \leq -\left(\kappa - \frac{\kappa^2\alpha^2}{\lambda_q}\right) \|\tilde{\boldsymbol{\omega}}\|^2 - \left(\sqrt{\lambda_q} \|\tilde{\mathbf{q}}_v\| + \frac{\kappa\alpha \|\tilde{\boldsymbol{\omega}}\|}{\sqrt{\lambda_q}}\right)^2 \quad (6.6)$$

Then, $\dot{V}(\boldsymbol{\eta})$ from Equation (6.6) is negative definite for $\kappa - \frac{\kappa^2\alpha^2}{\lambda_q} > 0$, showing that the candidate Lyapunov function $V(\boldsymbol{\eta})$ in Equation (6.1) is bounded in \mathcal{L}_∞ and that $V(\boldsymbol{\eta})$ is decreasing. From Equation (6.5) is inferred the error signals $\tilde{\boldsymbol{\omega}}, \tilde{\mathbf{q}}_v \in \mathcal{L}_2$, whereas $\tilde{\boldsymbol{\Theta}} \in \mathcal{L}_\infty$ meaning it remains bounded. Therefore, by invoking Barbalat's Lemma, it can be concluded that both the attitude and angular velocity of the spacecraft converge to the desired values since:

$$\lim_{t \rightarrow \infty} \begin{bmatrix} \tilde{\boldsymbol{\omega}} & \tilde{\mathbf{q}}_v \end{bmatrix} = 0 \quad (6.7)$$

□

Theorem 2. Consider the system described in Equation (4.13) with attitude dynamics described by Equation (2.7). Then the control law designed in Equation (5.8) and update law designed in Equation (5.10) guarantee global asymptotic stability for the attitude tracking error $\tilde{\mathbf{q}}_v$, the spacecraft angular velocity tracking error $\tilde{\boldsymbol{\omega}}$, and the error of the estimates of the unknown $\tilde{\boldsymbol{\Theta}}$ in a sense that $\lim_{t \rightarrow \infty} \begin{bmatrix} \tilde{\boldsymbol{\omega}} & \tilde{\mathbf{q}}_v & \tilde{\boldsymbol{\Theta}} \end{bmatrix} = 0$ for any $t_\lambda \leq t \leq \infty$.

Proof. Consider the extended state $\boldsymbol{\eta} = \begin{bmatrix} \tilde{\boldsymbol{\omega}}^T & \tilde{\mathbf{q}}_v^T & \tilde{\boldsymbol{\Theta}}^T \end{bmatrix}^T$ and let $V(\boldsymbol{\eta})$ be a positive definite Lyapunov's function defined as:

$$V(\boldsymbol{\eta}) = \frac{1}{2} \mathbf{r}^T P \mathbf{r} + \frac{1}{2} \tilde{\boldsymbol{\Theta}}^T \Gamma^{-1} \tilde{\boldsymbol{\Theta}} + \beta [\tilde{\mathbf{q}}_v^T \tilde{\mathbf{q}}_v + (\tilde{\mathbf{q}}_w - 1)^2] \quad (6.8)$$

and bounded by:

$$\gamma_1 \|\boldsymbol{\eta}\|^2 \leq V(\boldsymbol{\eta}) \leq \gamma_2 \|\boldsymbol{\eta}\|^2 \quad (6.9)$$

where γ_1 and γ_2 are positive bounding scalars. Substituting Equation (5.4), (5.5), (5.7), (5.8), and (5.10) in the first-time derivative of Equation (6.8) leads to:

$$\dot{V}(\boldsymbol{\eta}) = -\mathbf{r}^T(\kappa\tilde{\mathbf{r}} + \beta\tilde{\mathbf{q}}_v) + \beta\tilde{\mathbf{q}}_v^T\tilde{\boldsymbol{\omega}} - \tilde{\boldsymbol{\Theta}}^T K_{ICL}\tilde{\boldsymbol{\Theta}} \quad (6.10)$$

Since Equation (6.3) is not enough to show stability of the attitude mismatch and angular velocity error, the tracking signal \mathbf{r} is expanded in Equation (6.10) using (5.1), which yields:

$$\dot{V}(\boldsymbol{\eta}) = -\tilde{\boldsymbol{\omega}}^T \kappa \tilde{\boldsymbol{\omega}} - \tilde{\mathbf{q}}_v^T (\alpha\beta + \alpha^2\kappa) \tilde{\mathbf{q}}_v - 2\kappa\alpha\tilde{\boldsymbol{\omega}}^T \tilde{\mathbf{q}}_v - \tilde{\boldsymbol{\Theta}}^T K_{ICL}\tilde{\boldsymbol{\Theta}} \quad (6.11)$$

Further, Equation (6.11) can be upper-bounded using Hölder's inequality: $\|x^T y\| \leq \|x\| \|y\|$ as:

$$\dot{V}(\boldsymbol{\eta}) \leq -\kappa\|\tilde{\boldsymbol{\omega}}\|^2 - \lambda_q\|\tilde{\mathbf{q}}_v\|^2 - 2\kappa\alpha\|\tilde{\boldsymbol{\omega}}\| \cdot \|\tilde{\mathbf{q}}_v\| - \lambda_{ICL}\|\tilde{\boldsymbol{\Theta}}\|^2 \quad (6.12)$$

with λ_q equal to $(\alpha\beta + \alpha^2\kappa)$, and λ_{ICL} the minimum eigenvalue of K_{ICL} . Equation (6.12) can then be manipulated as:

$$\dot{V}(\boldsymbol{\eta}) \leq -\left(\kappa - \frac{\kappa^2\alpha^2}{\lambda_q}\right)\|\tilde{\boldsymbol{\omega}}\|^2 - \left(\sqrt{\lambda_q}\|\tilde{\mathbf{q}}_v\| + \frac{\kappa\alpha\|\tilde{\boldsymbol{\omega}}\|}{\sqrt{\lambda_q}}\right)^2 - \lambda_{ICL}\|\tilde{\boldsymbol{\Theta}}\|^2 \quad (6.13)$$

Then, $\dot{V}(\boldsymbol{\eta})$ from Equation (6.12) is negative definite for $\kappa - \frac{\kappa^2\alpha^2}{\lambda_q} > 0$, showing that the candidate Lyapunov function $V(\boldsymbol{\eta})$ in Equation (6.8) is bounded in \mathcal{L}_∞ and that $V(\boldsymbol{\eta})$ is decreasing. From Equation (6.12) is inferred the error signals $\tilde{\boldsymbol{\omega}}, \tilde{\mathbf{q}}_v, \tilde{\boldsymbol{\Theta}} \in \mathcal{L}_2$. Therefore, by invoking Barbalat's Lemma, it can be concluded that in addition to the results of Theorem 1 for attitude and angular velocity of the spacecraft, the update law with integral concurrent

learning will drive the estimates of the unknown parameters to their true value since since:

$$\lim_{t \rightarrow \infty} \tilde{\Theta} = 0 \quad (6.14)$$

□

7 Flexible Spacecraft Maneuvers

In this chapter, the performance of the designed controller in Equation (5.8) and update law in Equation (5.10) subject to the dynamics from Equation (4.13) is validated for two scenarios: the first one is to align the long axis of the flexible appendage with the relative linear velocity of the spacecraft as the system is following a circular orbit around Earth, and the second scenario is to perform set of arbitrary slew maneuvers. Furthermore, results of the response of the system and unknown estimations for different number of links modeled will be presented for comparison. For all scenarios, the P matrix of the Lyapunov function in Equation (6.1) is selected to be the principal moment of inertia of the main body J_H to provide a natural weighting of the angular velocity components due to the mass and dimensions of the spacecraft. The objective of the first scenario is to investigate how the proposed eigenvalue placement for the tuning matrix of the ICL-based adaptive law reacts as the number of modeled links for the same appendage is changed. The goal is to highlight the effectiveness of this approach to shape the behavior of the estimation of any number of unknowns. The objective of the second scenario is to investigate the behavior of the system in response to the adaptive law designed in Equation (5.10) and compare it to the response of a non-adaptive controller that does not estimate the unknown parameters. The goal is to highlight the advantage of implementing the ICL-based adaptive scheme in the controller for a flexible spacecraft.

7.1 Flexible appendage pointing to spacecraft relative velocity

7.1.1 Initial Conditions

Consider a 3U CubeSat that has been deployed from the International Space Station (ISS) and it has began its de-tumbling operation and that the deployment of the flexible appendage from the system has caused an initial tumble to it. The flexible appendage is assumed to be initially at rest and fully deployed, and the spacecraft has an initial tumble as described in Table 7.1. The mechanical properties like mass and dimensions for both the spacecraft hub and the flexible appendage are listed in Table 7.2. The inertial coordinate

system N is considered to be the one described by Earth-Centered Inertial (ECI).

Table 7.1 Initial Attitude, Position, and Velocities of the Spacecraft Hub

Initial Parameters	x	y	z	Units
$\mathbf{q}_v(0)$	-0.1344	-0.7317	0.6543	/
${}^N\mathbf{p}_H(0)$	7.5×10^3	0	0	km
${}^N\mathbf{v}_H(0)$	0	7.288	0	km/s
${}^N\boldsymbol{\omega}_H(0)$	0.100	-0.050	0.200	rad/s

Table 7.2 Mass and dimensions of the spacecraft bodies

Body	Mass (kg)	Height (m)	Length (m)	Width (m)
Hub	4.800	0.100	0.300	0.100
Appendage	0.113	0.050	1.500	5×10^{-4}

7.1.2 Desired Trajectory

Based on the initial position and velocity of the spacecraft, the initial values for propagating the desired attitude over time are selected by aligning the inertial x component with the body-fixed y component, the inertial y component with the opposite of the body-fixed x component, and the inertial z component with the body-fixed z component as shown in Figure 7.1, which results in $\mathbf{q}_{des}(0) = \begin{bmatrix} 0 & 0 & 1 & 0 \end{bmatrix}^T$. The desired angular velocity of the hub is obtained from the angular velocity of the circular orbit generated by the initial velocity and position from Table 7.1 and is ${}^D\boldsymbol{\omega}_{des}(0) = \begin{bmatrix} 0 & 0 & -9.972 \times 10^{-4} \end{bmatrix}^T rad/s$.

7.1.3 Controller Parameters

The number of data points collected for the integral concurrent learning is $N = 30$, which is collected using a window time of $\Delta t = 4t_s$, where t_s is the integration step size for the simulation. For actual controller implementation, it should match the time required to process the output measurements. The finite time excitation threshold is set to $\bar{\lambda} = 5 \times 10^{-3}$. A summary of the control gain matrices employed in the simulation is presented in Table 7.3. The control gain parameters κ , α , β , Γ are tuned to achieve the desired response. In particular, the first three gains: κ , α , β are responsible for the convergence rate of the error

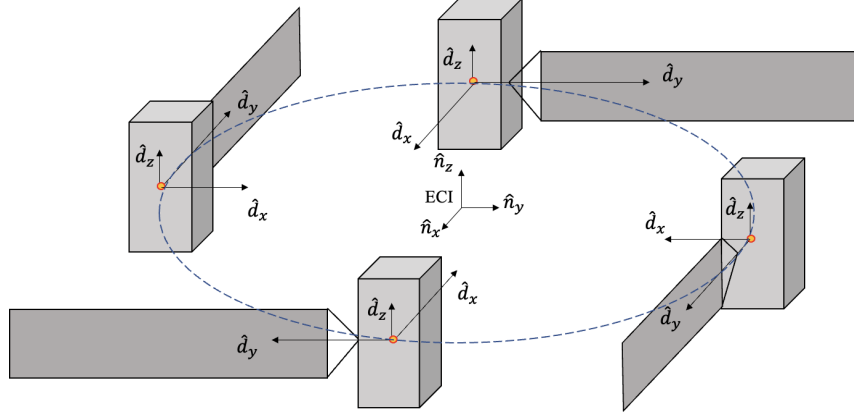


Figure 7.1 Visual Representation of desired trajectory for scenario 1. The flexible appendage is aligned with the velocity vector of the circular orbit around Earth, always facing normal to Earth.

Table 7.3 Control Gains Parameters

κ	α	β	Γ	Σ_{des}	N	λ
0.01	0.15	0.0025	1.25	$1 \leq \sigma_i \leq 10$	30	5×10^{-3}

in the angular velocity of the hub and its attitude as shown in Equation (6.4), whereas Γ plays a role in the finite time excitation of the system for estimation of the unknowns as shown in Equation (5.10). Λ from Equation (6.11) dictates the convergence rate of the error in the unknown parameters. However, since the only tune-able parameters of Λ are the desired singular values for the ICL learning matrix, they are selected from a random normal Gaussian distribution from 1 to 10, and diagonalized in Σ_{des} .

7.1.4 Simulation Results

Using a 4th order Runge-Kutta solver with integration fixed size of $dt = 0.005$ s, a simulation of the dynamics of the spacecraft described in Equation (4.1) with the control law in Equation (5.8) and the adaptive law in Equation (5.10) is performed. The initial estimates of the unknowns $\hat{\Theta}$ were all set to zero to provide a worst-case scenario where the joints do not apply torques on the structure. The response of the system is obtained for a flexible appendage modeled as $n = 3, 6, 12$ links.

For all three cases, the controlled maneuver drove the attitude of the spacecraft and

angular velocity to the desired trajectory while following a circular orbit around Earth as shown in Figure 7.2. This can be confirmed by the mean of both $\tilde{\omega}$ and $\tilde{\mathbf{q}}_v$ reaching values less than 1×10^{-5} . Because the flexible appendage is more accurately modeled as the number of links increases, the tracking error improves since it approaches values closer to zero. Furthermore, the flexible appendage shows an initial excitation for the first oscillations due to the mismatch in the estimates of the unknowns, and for higher number of links, the excitation is more accentuated as shown in Figure 7.3. Once the learning phase is completed, the appendage dampens down to steady-state and the decay rate for which it happens is slower for larger number of links.

An insightful result is that the controller was able to meet the attitude tracking objective before the flexible appendage reached steady-state. That is because the controller has estimated spring and damping coefficients almost true to their actual values, meaning that is able to compensate for the oscillations of the appendage while maintaining the desired attitude, which can be observed from the behavior of the controller input over time in Figure 7.4. In fact, the estimates of the unknown parameters reach a relative percent error of less than 1% as shown in Table 7.4, meaning that the update law with Integral Concurrent Learning and the self-adjusting tuning proposed in this paper is effective to accurately estimate constant unknowns that can be linearly parameterized from the dynamics of the system. The magnitude of the percent errors from Table 7.4 can be attributed to small numerical errors due to the collection of the integrals \mathcal{Y}_i and \mathcal{U}_i which are propagated in the sum $\sum \mathcal{Y}_i^T \mathcal{Y}_i$. The finite excitation stage and the convergence stage of the ICL are distinguishable from Figure 7.5 and 7.6, which indicates the minimum eigenvalue condition in Equation (5.16) has been met.

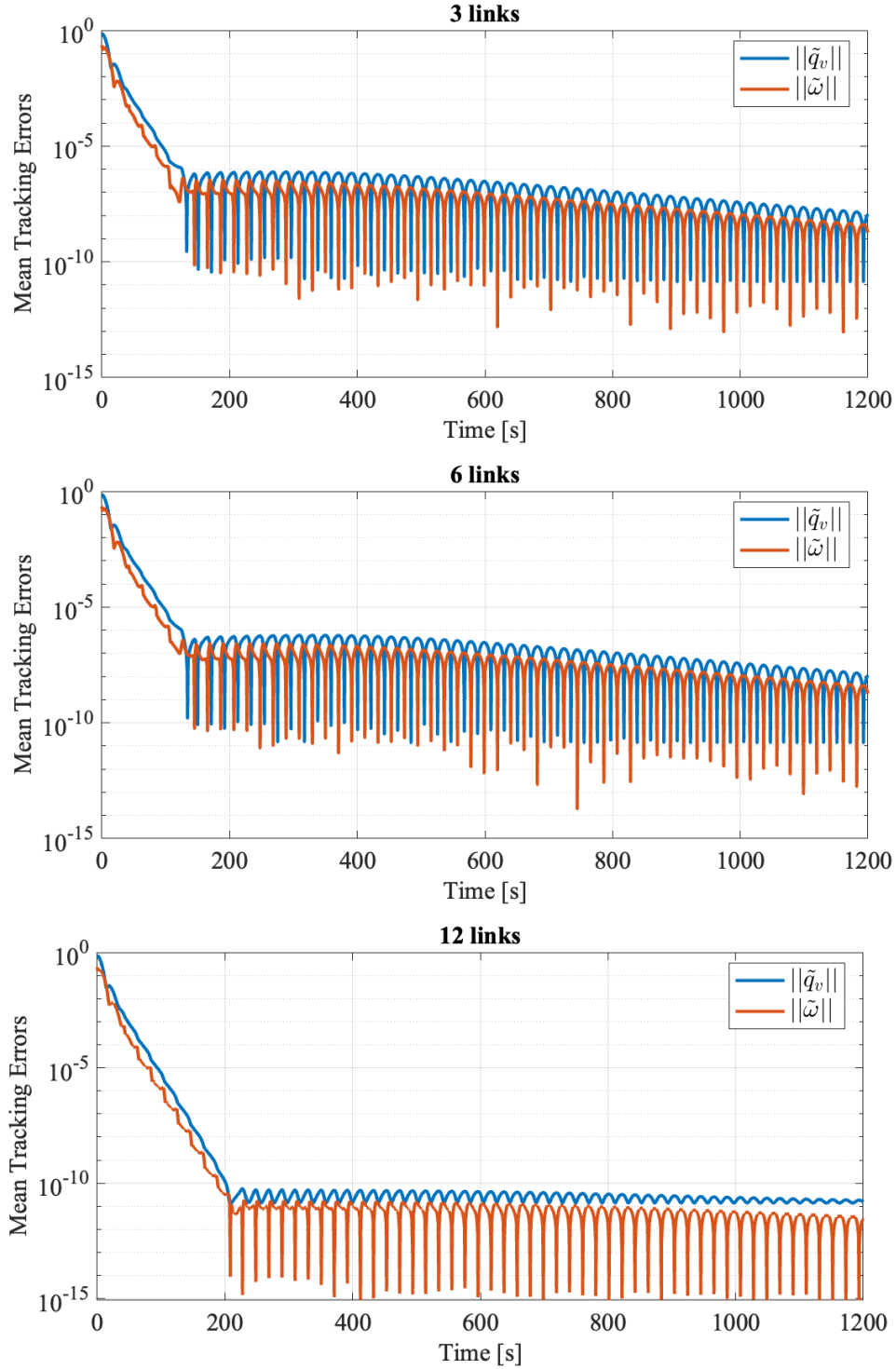


Figure 7.2 Behavior of the tracking error represented as the mean of the attitude mismatch and spacecraft angular velocity error over a time span of 1200s. Both errors converge closer to zero as the number of links increases.

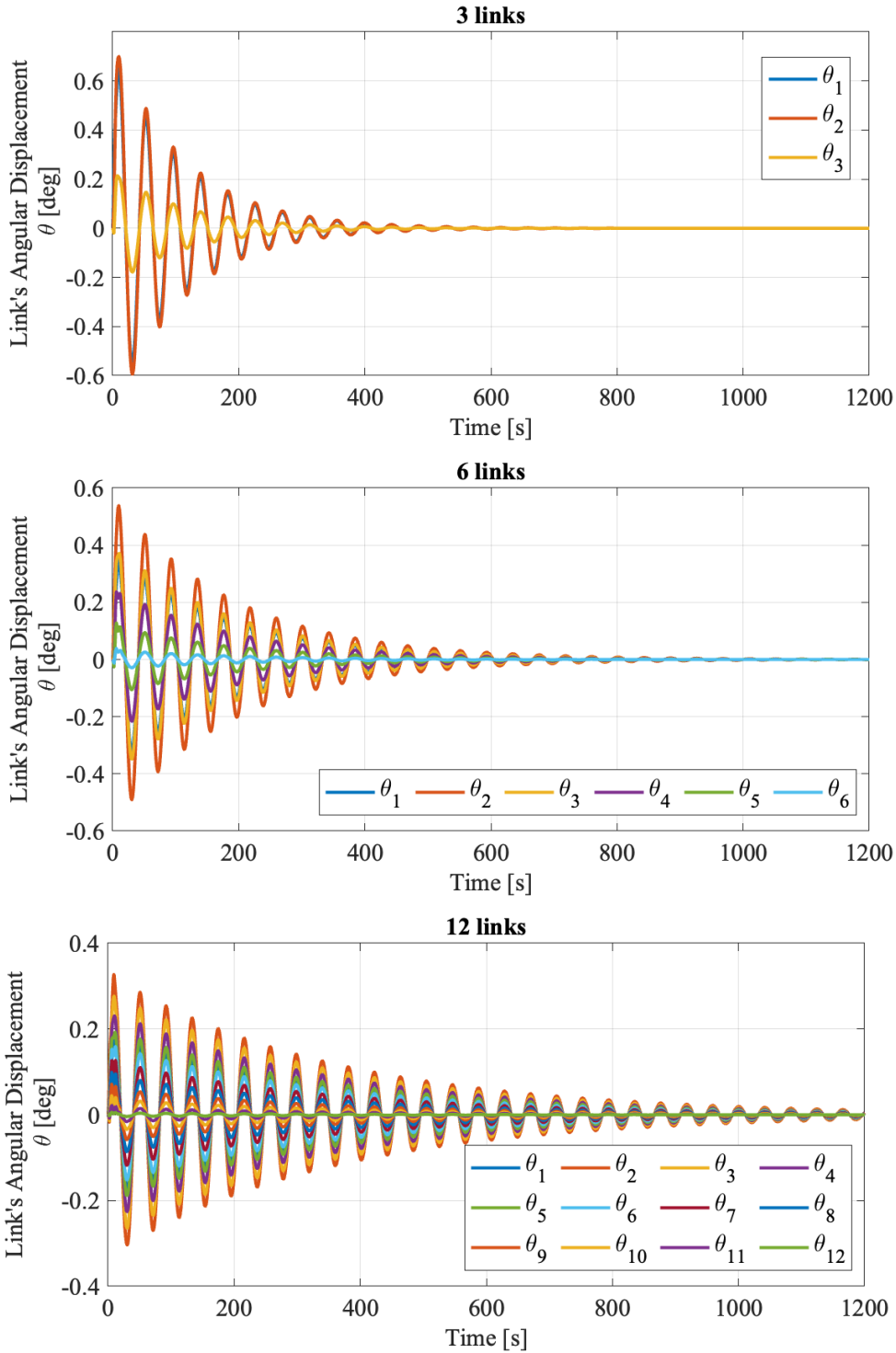


Figure 7.3 Behavior of the relative angular displacements of each link over a time-span of 1200s. The excitation phase of the update law emphasizes the initial oscillations of the appendage as the number of links increases. However, once the estimates of the unknowns reach their true values, the frequency of the oscillations remains constant and the decaying rate of the waves is slower as n increases.

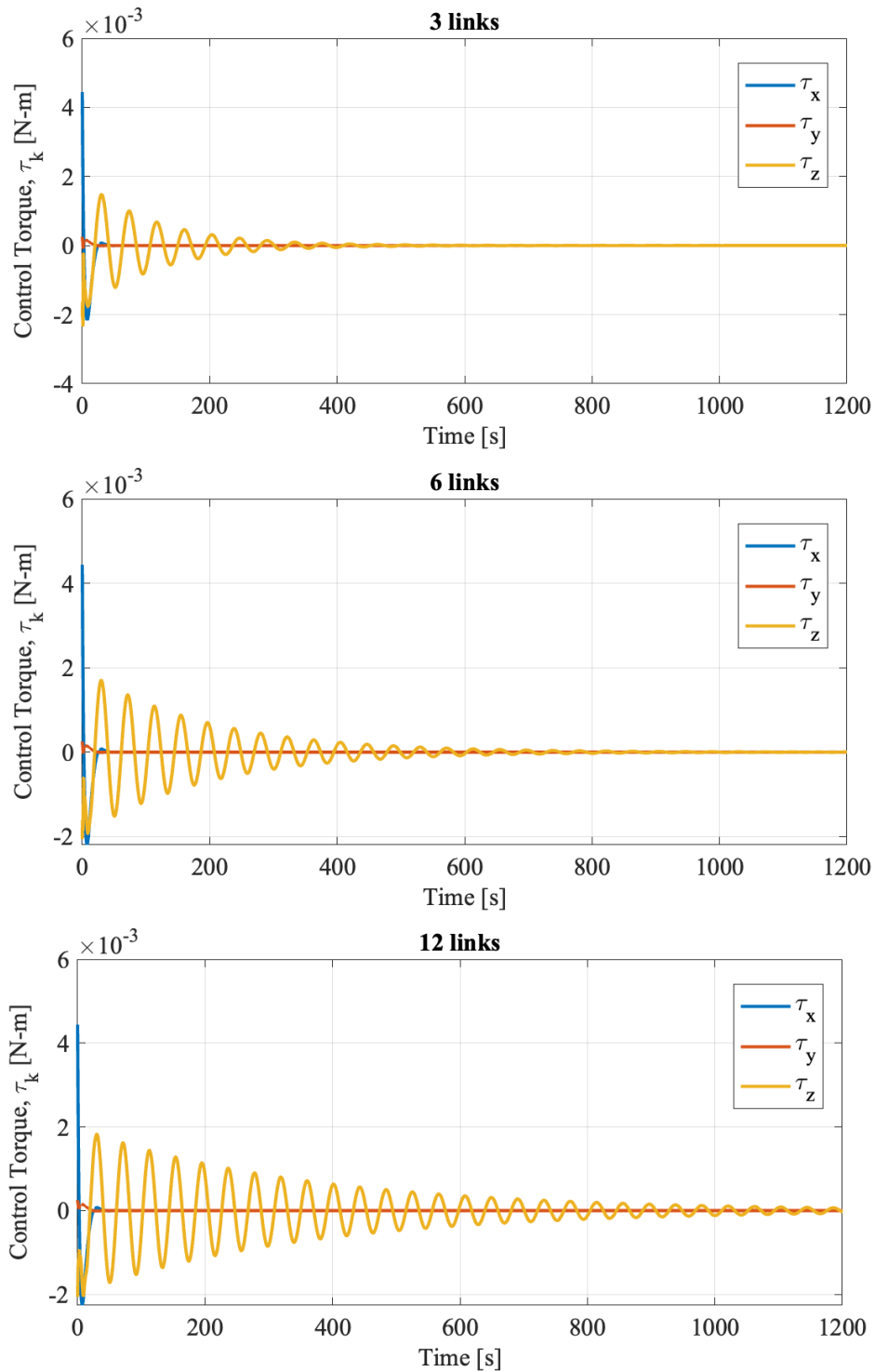


Figure 7.4 Behavior of the input commanded torques to the spacecraft hub over a time-span of 1200s. As the number of links increases, the behavior of the controller reflects the oscillations of the flexible appendage to maintain the desired attitude trajectory.

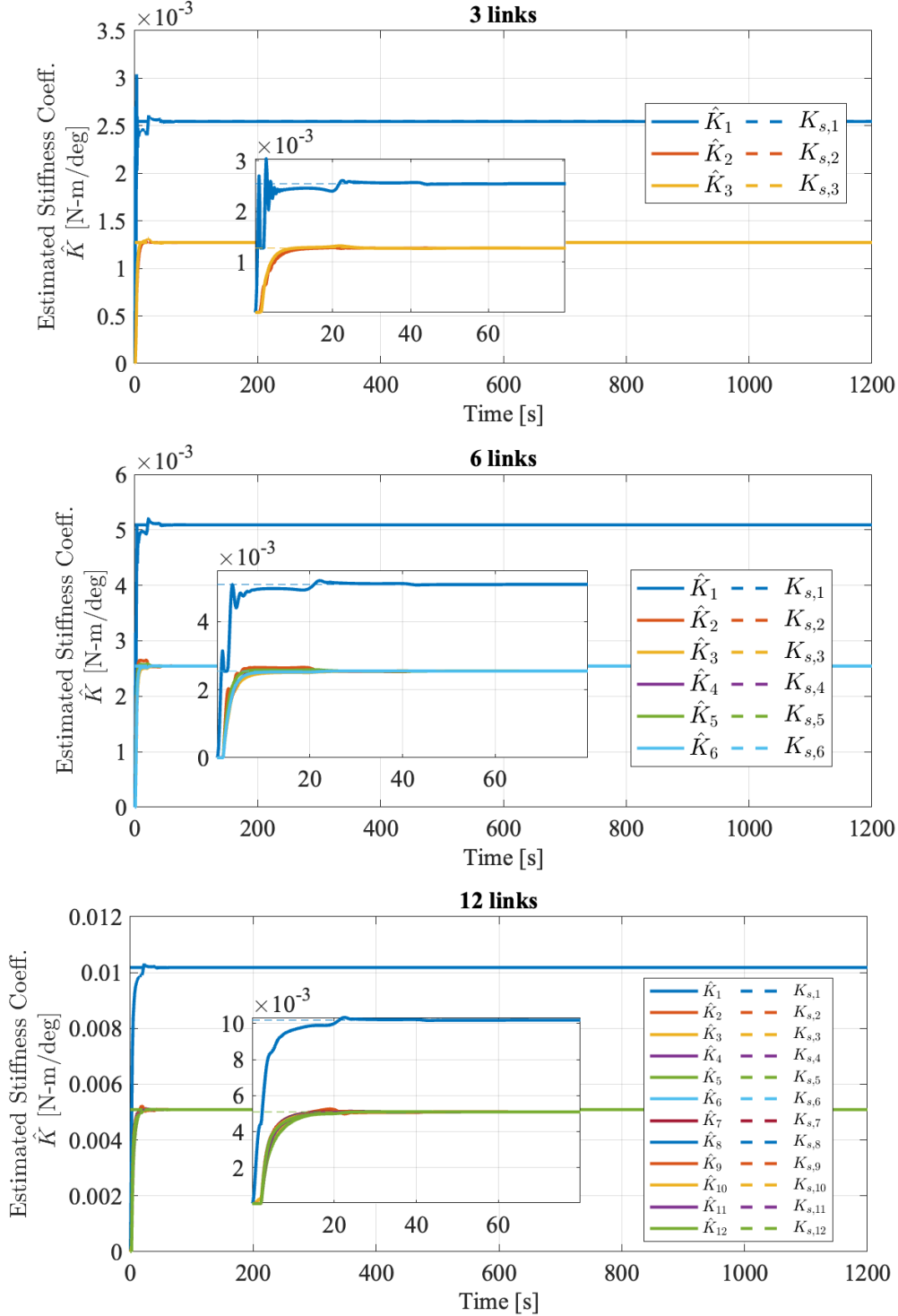


Figure 7.5 Behavior of the estimated spring coefficients compared to their actual values over a time-span of 1200s. The controller with ICL accurately estimates the unknown spring coefficients after the initial finite excitation that lasts about 20 seconds. For constant tuning parameter Γ for all three models, the excitation applied to the estimates of the unknown spring coefficients is less aggressive as the number of unknowns increases, but still sufficient to collect information for the learning matrix to drive the estimates to their true values.

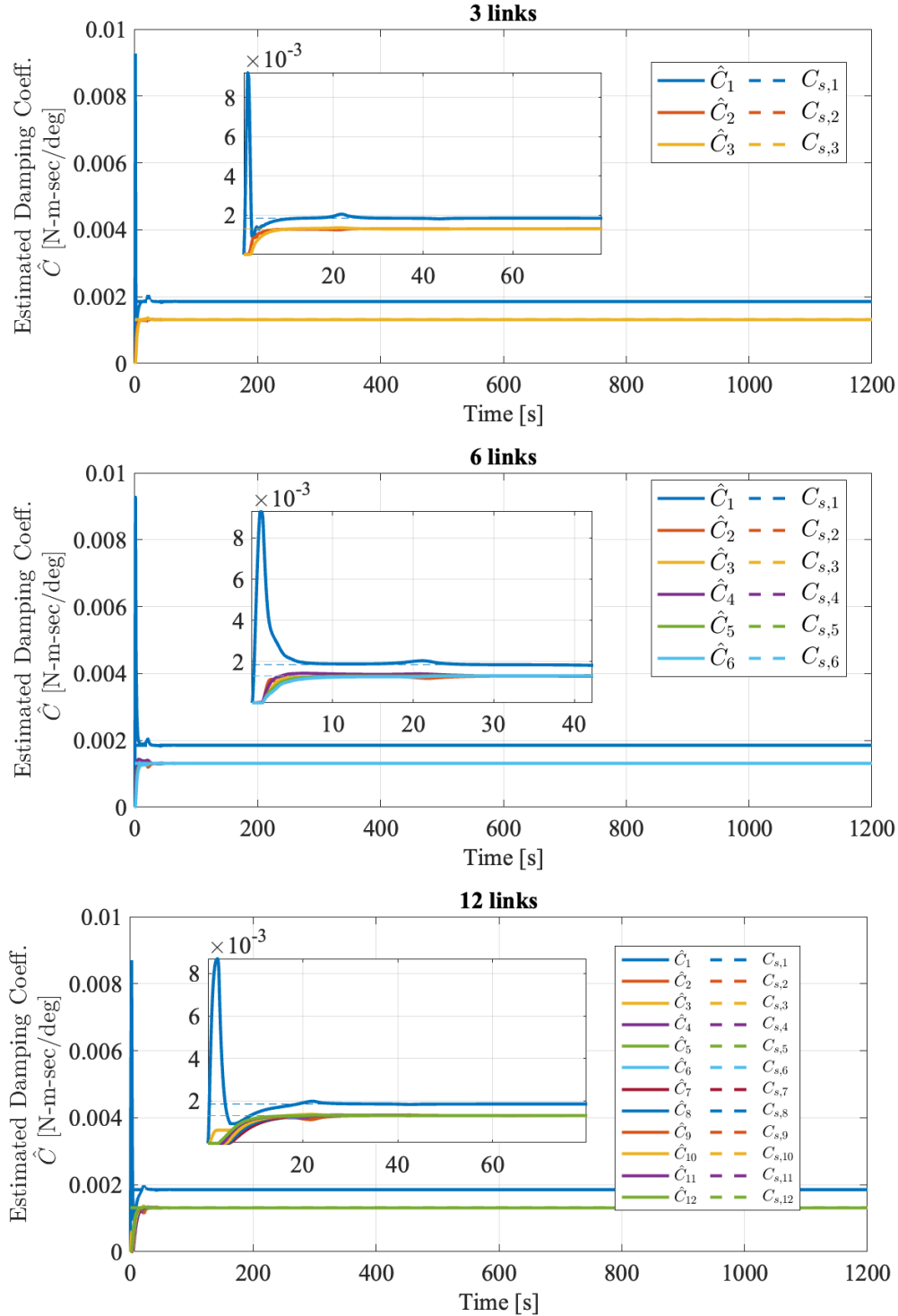


Figure 7.6 Behavior of the estimated damping coefficients compared to their actual values over a time-span of 1200s. The controller with ICL accurately estimates the unknown damping coefficients after the initial finite excitation that lasts about 20 seconds. For constant tuning parameter Γ for all three models, the excitation applied to the estimates of the unknown damping coefficients does not show a significant difference as the number of unknowns increases.

Table 7.4 Relative percent error of the final unknown estimates for different number of links modeled

Number links modeled	$n = 3$		$n = 6$		$n = 12$	
Unknown Error	$\tilde{\mathbf{k}}_i$	$\tilde{\mathbf{c}}_i$	$\tilde{\mathbf{k}}_i$	$\tilde{\mathbf{c}}_i$	$\tilde{\mathbf{k}}_i$	$\tilde{\mathbf{c}}_i$
1st link	0.887%	0.145%	0.013%	0.209%	0.007%	0.068%
2nd + links	0.094%	0.007%	0.303%	0.256%	0.148%	0.043%

7.2 Slew-Maneuvers

Initial Conditions

Consider the same spacecraft from Section 7.1 with the same initial conditions and mechanical properties described in Table 7.1 and 7.2 respectively. The flexible appendage is modeled as $n = 5$ links for both cases. The initial estimates of the unknowns $\hat{\mathbf{k}}$ and $\hat{\mathbf{c}}$ are described in Table 7.5 and they represent an initial wrong assumption of the joint springs and dampers.

Table 7.5 Initial estimates of the unknowns and their constant true values

Parameter	$j = 1$	$j = 2$	$j = 3$	$j = 4$	$j = 5$	Units
k_j	0.00424	0.00212	0.00212	0.00212	0.00212	$N - m/deg$
$\hat{k}_j(0)$	0.00246	0.00209	0.00208	0.00158	0.00191	$N - m/deg$
c_j	0.00185	0.00131	0.00131	0.00131	0.00131	$N - m - sec/deg$
$\hat{c}_j(0)$	0.00106	0.000932	0.00126	0.00117	0.00128	$N - m - sec/deg$

7.2.1 Desired Trajectory

To perform slew maneuvers, the desired attitude parameters \mathbf{q}_{des} are changed every 200 s by performing one rotation of an angle about one axis and a visualization of the desired maneuvers is shown in Figure 7.7. The trajectory map is selected as:

$$\mathbf{q}_{des} = \begin{cases} \begin{bmatrix} 0 & 1 & 0 & 0 \end{bmatrix}^T & 0 \leq t < 200s \\ \begin{bmatrix} 0.5000 & 0 & 0 & 0.8660 \end{bmatrix}^T & 200 \leq t < 400s \\ \begin{bmatrix} 0 & 0 & -0.3827 & 0.9239 \end{bmatrix}^T & 400 \leq t < 600s \\ \begin{bmatrix} 1 & 0 & 0 & 0 \end{bmatrix}^T & t > 600s \end{cases} \quad (7.1)$$

The desired angular velocity of the hub is set to zero in order to maintain a constant target attitude even when it is switching.

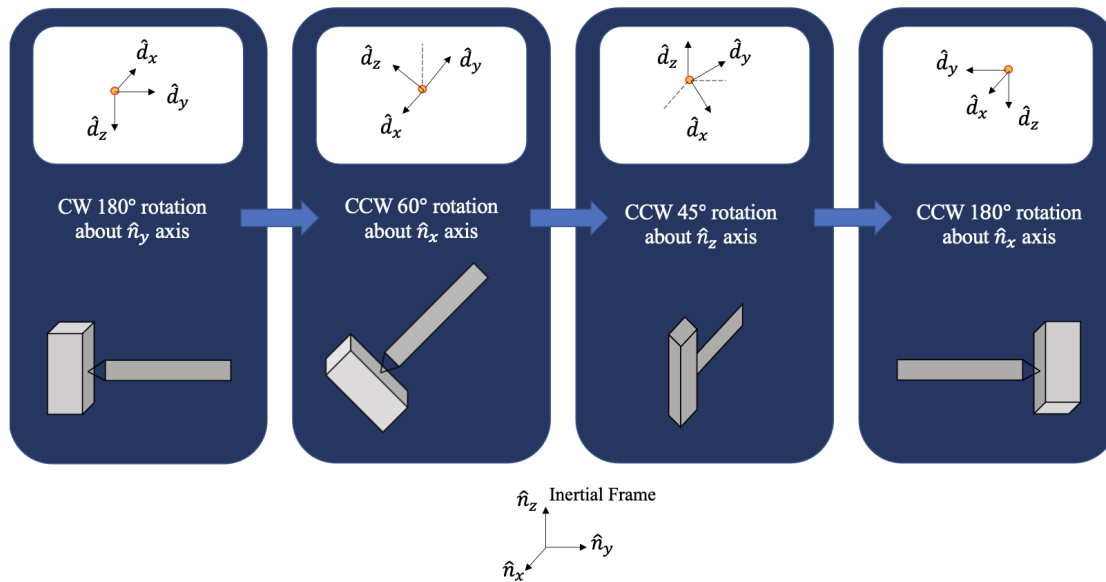


Figure 7.7 Visual representation of the desired slew maneuvers performed every 200 seconds.

7.2.2 Simulation Results

Using a 4th order Runge-Kutta solver with fixed step size of $dt = 0.005$ s, a simulation of the dynamics of the spacecraft described in Equation (4.1) with the control law in Equation (5.8), control tuning parameters defined in Table 7.3 and desired attitude maneuvers defined in Equation (7.1) is performed.

The significant difference between the two cases is that the estimation of the unknowns was obviously accurately met by the ICL-based adaptive law as shown in Figure 7.8, whereas the estimates for the second case were not updated and kept constant with values described by Table 7.5. The mean error of the quaternion and angular velocity for both cases is depicted in Figure 7.9. Without estimation, the controller does not achieve good tracking by the time the next maneuver is requested. The response of the displacements of the flexible appendage is shown in Figure 7.10, and it shows the expected mismatch in flexible dynamics for oscillations amplitude and decay due to the non-adaptive controller constantly using the

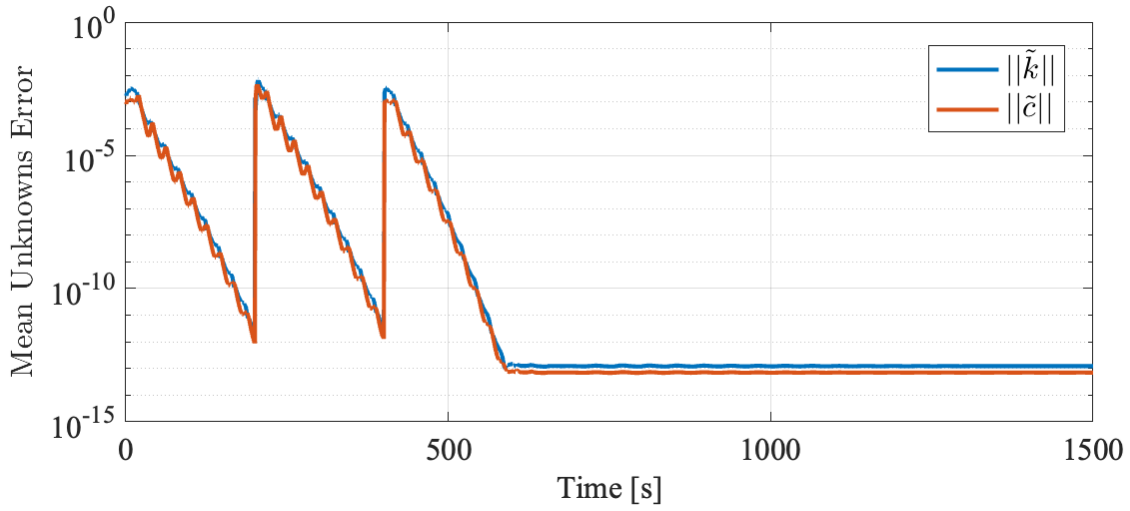


Figure 7.8 Mean error of the unknown parameters over a time-span of 1500s. The estimates of the unknowns accurately reach their true value for each maneuver as the magnitude of the mean error between actual and estimated values converges to 1×10^{-12} at the end of each maneuver.

wrong estimates for the spring and damping coefficients of the joints. The same behavior is appreciated by the commanded input torques over time that reflects the magnitude of the oscillations of the flexible appendage as shown in Figure [7.11](#).

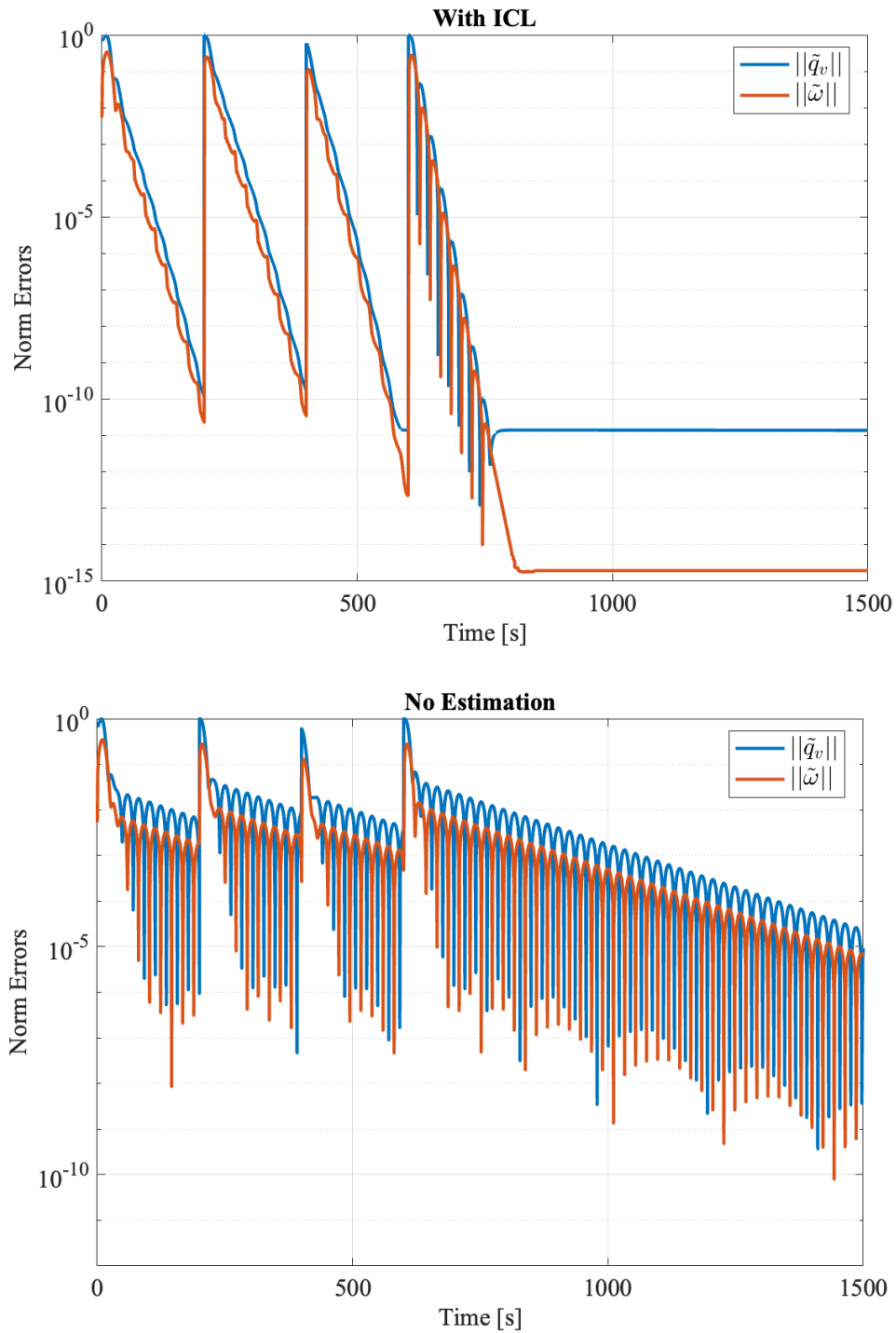


Figure 7.9 Behavior of the tracking error for the second scenario represented by the attitude mismatch and spacecraft angular velocity error over a time span of 1500s. By the end of each maneuver, the mean of both errors for the controller with ICL converges closer to zero than the one of the non-adaptive controller.

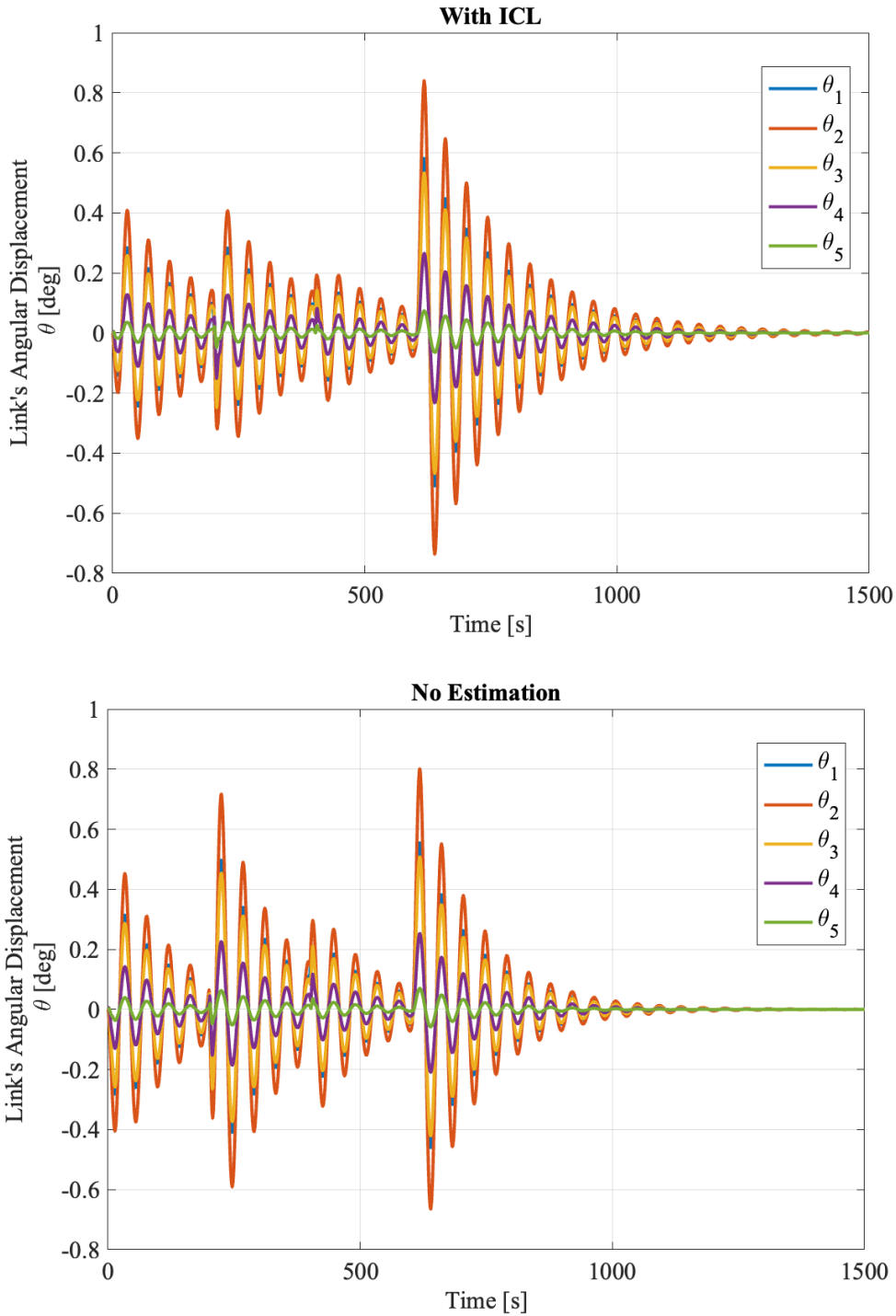


Figure 7.10 Behavior of the relative angular displacements of each link for the second scenario over a time-span of 1500s. The oscillations of the flexible appendage controlled by a non-adaptive law have a higher decay rate than the ones controlled by the ICL-based adaptive law. However, a higher wave amplitude is observed for the first three maneuvers when the control law does not use the correct estimates of the unknown spring and damping coefficients.

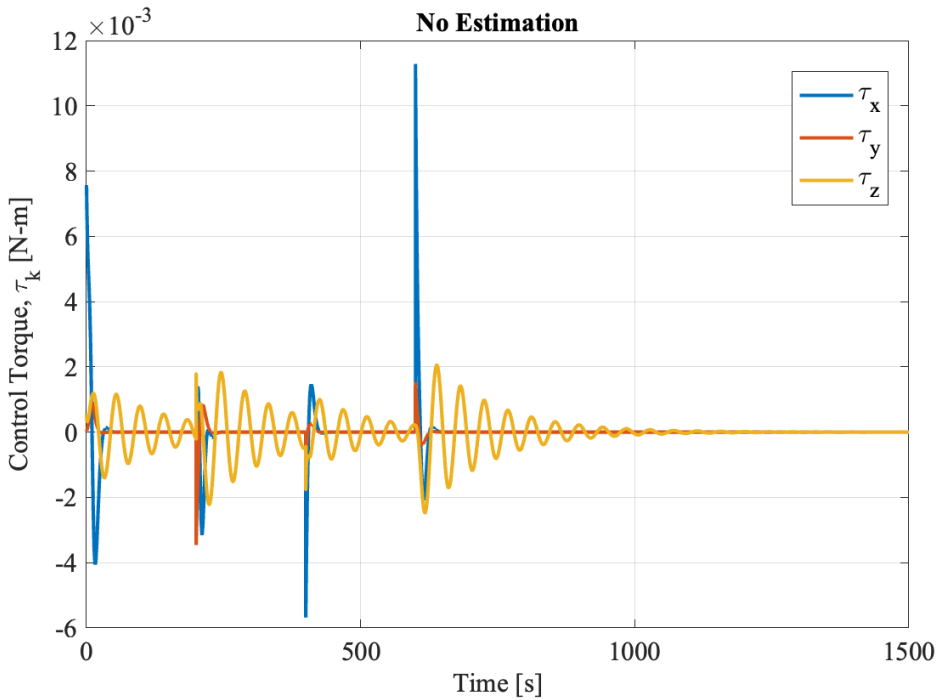
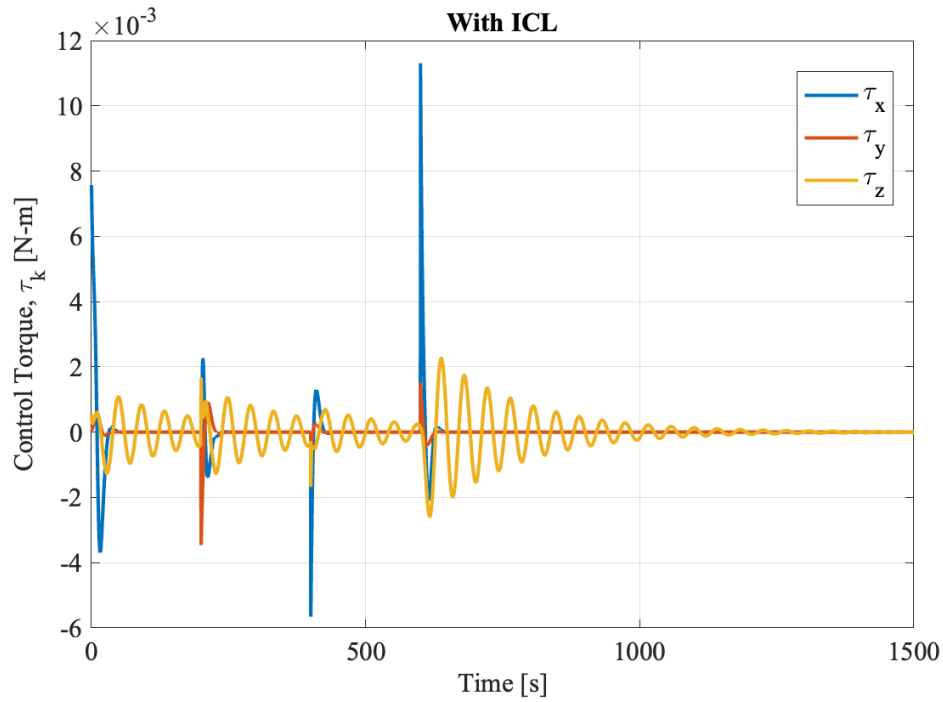


Figure 7.11 Behavior of the input commanded torques on the spacecraft hub for the second scenario over a time-span of 1500s. For both cases of the second scenario, the x and y component of the torques do not differ, whereas the z component of the non-adaptive controller shows higher magnitude for the first three maneuvers which reflects the behavior of the flexible appendage.

8 Discussion

Both scenarios have yielded the expected results and validated the theorems of stability introduced in Chapter 6. That is the controller and adaptive law designed in Equation (5.8) and (5.10) for the system in Equation (4.1) is able to drive the spacecraft attitude and angular velocity to a desired one, and accurately estimate the unknown parameters.

In Scenario 1, the performance of the control and adaptive law was presented when the flexible appendage was modeled with a different number of rigid links. The results were satisfactory since the proposed approach of self-tuning the eigenvalues of the learning matrix allowed estimating unknowns of an appendage modeled with higher number of links, improving accuracy and identification of modes of frequency. Furthermore, since the spring and damping coefficients are concurrently estimated, the proposed algorithm would be able to capture the changes in the actual coefficients when other modes are excited. That is because the natural frequency of the i th mode is determined as shown in Reference [17]:

$$\omega_i = (\beta L)^2 \sqrt{\frac{EI}{\rho L^4}} = \sqrt{\frac{k_i}{m}} \quad (8.1)$$

with (βL) being the solution of the characteristic equation of the shape function (Equation 4.45 in Reference [17]), L being the length of the beam, ρ being the density of the material. The Lyapunov-based controller drives the spacecraft hub to its desired attitude and angular velocity even when the flexible appendage is still oscillating. The control objective is met thanks to the accurate estimation of the underactuated unknown dynamics because the controller compensates for that dynamics and maintains the desired trajectory. This conclusion is discerned from the results of the last scenario since it was observed the non-adaptive controller cannot accurately drive the spacecraft to the desired orientation and angular velocity in the required time for the maneuver. This response is due to the uncertainty in the modeled flexible dynamics; therefore, the control input applied to the spacecraft results in residual torques the controller does not compensate for. The motivation behind accurately

estimating the dynamics of the flexible appendage is to, in fact, being able to select the appropriate controller. A mismatch between the actual dynamics of the flexible appendage and the one assumed from the controller could generate an uncontrollable excitation because it could exceed the frequency bandwidth of the controller, or not meeting the control tracking objective because of the poor modeling. Furthermore, the improvement provided in the current ICL scheme of implementing a self-tuning gain matrix shows that a better performance for the estimation algorithm can be included for larger number of unknowns. In both scenarios, constraints and limitations on the control input were not imposed, but for a real mission, considerations on the maximum required torques, frequency bandwidths, time-delays and other mechanical constraints imposed by the proposed controller unit must be taken into account.

9 Conclusions

In conclusion, modeling the spacecraft with a flexible appendage by considering the flexible component as a finite series of rigid bodies connected by torsional joints is selected as a method to estimate the unknown flexible dynamics by performing an onboard estimation of unknown parameters of the flexible joints using integral concurrent learning. Two scenarios of desired trajectories were tested: a smooth time-varying trajectory in Scenario 1 and a switched trajectory in Scenario 2. The results from the first scenario showed that the designed self-tuning control gain matrix allows for accurate and improved estimation of any number of unknown parameters in the system without exceeding the estimation bounds and guaranteeing a uniform convergence rate for all the unknowns. Furthermore, the results from the second scenario showed that estimating the unknowns is necessary for achieving the control objective of tracking a desired attitude trajectory in a fixed amount of time. Moreover, learning about the flexible dynamics helps with determining the controller design requirements like maximum output torque and frequency bandwidth, and it opens opportunities for accurately maneuvering the flexible appendage. Future works include testing the proposed theory in an experimental environment subject to measurement noise and time delays, and considering size and mass of the flexible appendage as unknowns. A further investigation will be applying to a continuous flexible appendage and using the discretized model for unknown estimation

REFERENCES

- [1] Xiao, B., Hu, Q., and Friswell, M. I., “Active fault-tolerant attitude control for flexible spacecraft with loss of actuator effectiveness,” *International Journal of Adaptive Control and Signal Processing*, Vol. 27, No. 11, 2013, pp. 925–943. <https://doi.org/https://doi.org/10.1002/acs.2363>.
- [2] Du, H., Chen, M. Z. Q., and Wen, G., “Leader–Following Attitude Consensus for Spacecraft Formation with Rigid and Flexible Spacecraft,” *Journal of Guidance, Control, and Dynamics*, Vol. 39, No. 4, 2016, pp. 944–951. <https://doi.org/https://doi.org/10.2514/1.G001273>.
- [3] Zhang, Z., Qi, Z., Wu, Z., and Fang, H., “A Spatial Euler-Bernoulli Beam Element for Rigid-Flexible Coupling Dynamic Analysis of Flexible Structures,” *Shock and Vibration*, Vol. 2015, 2015. <https://doi.org/https://doi.org/10.1155/2015/208127>, URL <http://ezproxy.libproxy.db.erau.edu/login?url=https://www.proquest.com/scholarly-journals/spatial-euler-bernoulli-beam-element-rigid/docview/1702178870/se-2>, name - Dalian University of Technology; Copyright - Copyright © 2015 Zhigang Zhang et al. Zhigang Zhang et al. This is an open access article distributed under the Creative Commons Attribution License, which permits unrestricted use, distribution, and reproduction in any medium, provided the original work is properly cited; Last updated - 2018-10-16.
- [4] Liu, F., Yue, B., and Zhao, L., “Attitude dynamics and control of spacecraft with a partially filled liquid tank and flexible panels,” *Acta Astronautica*, Vol. 143, 2018, pp. 327–336. <https://doi.org/https://doi.org/10.1016/j.actaastro.2017.11.036>, URL <https://www.sciencedirect.com/science/article/pii/S0094576517311232>.
- [5] Kane, T. R., and Levinson, D. A., “Formulation of Equations of Motion for Complex Spacecraft,” *Journal of Guidance and Control*, Vol. 3, No. 2, 1980, pp. 99–112. <https://doi.org/10.2514/3.55956>, URL <https://doi.org/10.2514/3.55956>.

- [6] Talaeizadeh, A., Forootan, M., Zabihi, M., and Nejat Pishkenari, H., “Comparison of Kane’s and Lagrange’s Methods in Analysis of Constrained Dynamical Systems,” *Robotica*, Vol. 38, No. 12, 2020, p. 2138–2150. <https://doi.org/10.1017/S0263574719001899>.
- [7] Pishkenari, H. N., Yousefsani, S. A., Gaskarimahalle, A. L., and Oskouei, S. B. G., “A fresh insight into Kane’s equations of motion,” *Robotica*, Vol. 35, No. 3, 2017, pp. 498–510. <https://doi.org/https://doi.org/10.1017/S026357471500065X>.
- [8] Stoneking, E., *Implementation of Kane’s Method for a Spacecraft Composed of Multiple Rigid Bodies*, chapter and pages. <https://doi.org/10.2514/6.2013-4649>, URL <https://arc.aiaa.org/doi/abs/10.2514/6.2013-4649>.
- [9] Bell, K. D., Moser, R. L., Powers, M. K., and Erwin, R. S., “Deployable optical telescope ground demonstration,” *UV, Optical, and IR Space Telescopes and Instruments*, Vol. 4013, edited by J. B. Breckinridge and P. Jakobsen, International Society for Optics and Photonics, SPIE, SPIE Digital Library, 2000, pp. 559 – 567. <https://doi.org/10.1117/12.393995>.
- [10] Ioannou, P. A., and Sun, J., *Robust adaptive control*, Courier Corporation, New York, 2012.
- [11] Chowdhary, G. V., and Johnson, E. N., “Theory and flight-test validation of a concurrent-learning adaptive controller,” *Journal of Guidance, Control, and Dynamics*, Vol. 34, No. 2, 2011, pp. 592–607. <https://doi.org/https://doi.org/10.2514/1.46866>.
- [12] Parikh, A., Kamalapurkar, R., and Dixon, W. E., “Integral concurrent learning: Adaptive control with parameter convergence using finite excitation,” *International journal of adaptive control and signal processing*, Vol. 33, No. 12, 2019, pp. 1775–1787. <https://doi.org/https://doi.org/10.1002/acs.2945>.
- [13] Riano-Rios, C., Bevilacqua, R., and Dixon, W. E., “Differential drag-based multiple spacecraft maneuvering and on-line parameter estimation using integral concur-

- rent learning,” *Acta astronautica*, Vol. 174, 2020, pp. 189–203. <https://doi.org/https://doi.org/10.1016/j.actaastro.2020.04.059>.
- [14] Banerjee, A. K., *Flexible Multibody Dynamics : Efficient Formulations and Applications*, John Wiley & Sons, Incorporated, New York, UNITED KINGDOM, 2016. URL <http://ebookcentral.proquest.com/lib/erau/detail.action?docID=4454415>.
- [15] Nguyen, K.-D., and Dankowicz, H., “Adaptive control of underactuated robots with unmodeled dynamics,” *Robotics and autonomous systems*, Vol. 64, 2015, pp. 84–99. <https://doi.org/https://doi.org/10.1016/j.robot.2014.10.009>.
- [16] Chowdhary, G., and Johnson, E., “A singular value maximizing data recording algorithm for concurrent learning,” *Proceedings of the 2011 American Control Conference*, IEEE, San Francisco, CA, 2011, pp. 3547–3552. <https://doi.org/https://doi.org/10.1109/ACC.2011.5991481>.
- [17] Junkins, J. L., *Introduction to dynamics and control of flexible structures*, AIAA education series, American Institute of Aeronautics and Astronautics, Inc., Washington, D.C, 1993. <https://doi.org/https://doi.org/10.2514/4.862076>.

PUBLICATIONS

Woodward, N., Bevilacqua, R., Sinclair A., (2023, January 14-20). *Online Estimation of Unknown Parameters of Highly Flexible Spacecraft using Integral Concurrent Learning and Kane's Equation* [Paper presentation]. 33rd AAS/AIAA Space Flight Mechanics Meeting, Austin, TX, United States

A Appendix

A.1 Partial velocity matrices

The angular partial velocity matrix Ω is obtained as:

$$\Omega = \begin{bmatrix} I_3 & 0 & 0 & 0 & 0 & 0 \\ R^{H \rightarrow 1} & \Psi & 0 & 0 & 0 & 0 \\ R^{H \rightarrow 2} & R^{1 \rightarrow 2} \Psi & \Psi & 0 & 0 & 0 \\ \vdots & \vdots & \vdots & \ddots & 0 & 0 \\ R^{H \rightarrow n} & R^{1 \rightarrow n} \Psi & \dots & R^{n-1 \rightarrow n} \Psi & \Psi & 0 \end{bmatrix} \quad (\text{A.1})$$

The linear velocity matrix V is obtained as:

$$V = \begin{bmatrix} 0 & 0 & \dots & 0 & I_3 \\ \left({}^N \mathbf{r}_{L1 \rightarrow J1} - {}^N \mathbf{r}_{H \rightarrow J1} \right)^\times R^{H \rightarrow N} & \left({}^N \mathbf{r}_{L1 \rightarrow J1} \right)^\times R^{1 \rightarrow N} \Psi & 0 & 0 & I_3 \\ \vdots & \vdots & \ddots & 0 & I_3 \\ \left({}^N \mathbf{r}_{Ln \rightarrow J1} - {}^N \mathbf{r}_{H \rightarrow J1} \right)^\times R^{H \rightarrow N} & \left({}^N \mathbf{r}_{Ln \rightarrow J1} \right)^\times R^{1 \rightarrow N} \Psi & \dots & \left({}^N \mathbf{r}_{Ln \rightarrow Jn} \right)^\times R^{n \rightarrow N} \Psi & I_3 \end{bmatrix} \quad (\text{A.2})$$

where the vector $\mathbf{x}_{Li \rightarrow Jk}$ is the path vector from the center of mass of link i to the k th joint, for $i = 1 : n$ and $k = 1 : n - 1$ with n being the number of links modeled.

The time-derivative of Ω is calculated as:

$$\dot{\Omega} = \begin{bmatrix} 0_3 & 0 & 0 & 0 & 0 & 0 \\ \dot{R}^{H \rightarrow 1} & 0 & 0 & 0 & 0 & 0 \\ \dot{R}^{H \rightarrow 2} & \dot{R}^{1 \rightarrow 2} \Psi & 0 & 0 & 0 & 0 \\ \vdots & \vdots & \vdots & \ddots & 0 & 0 \\ \dot{R}^{H \rightarrow n} & \dot{R}^{1 \rightarrow n} \Psi & \dots & \dot{R}^{n-1 \rightarrow n} \Psi & 0 & 0 \end{bmatrix} \quad (\text{A.3})$$

where $\dot{R}^{i \rightarrow j} = \dot{R}^{i \rightarrow j} ({}^i \boldsymbol{\omega}^{i \rightarrow j})^\times$ read as the cross product between the transformation matrix from frame i to frame j with the angular velocity of the two frames expressed in the i frame.

The time-derivative of V is calculated as:

$$\dot{V} = \begin{bmatrix} 0 & 0 & 0 & 0 & 0 \\ \dot{V}_{10} & \dot{V}_{11} & 0 & 0 & 0 \\ \vdots & \vdots & \ddots & 0 & 0 \\ \dot{V}_{n0} & \dot{V}_{n1} & \cdots & \dot{V}_{nn} & 0 \end{bmatrix} \quad (\text{A.4})$$

with each element determined as:

$$\dot{V}_{i0} = \left({}^N \dot{\mathbf{r}}_{Li \rightarrow J1} - {}^N \dot{\mathbf{r}}_{H \rightarrow J1} \right)^\times R^{H \rightarrow N} + \left({}^N \mathbf{r}_{Li \rightarrow J1} - {}^N \mathbf{r}_{H \rightarrow J1} \right)^\times \dot{R}^{H \rightarrow N} \quad (\text{A.5})$$

$$\dot{V}_{ik} = \left({}^N \dot{\mathbf{r}}_{Li \rightarrow Jk} \right)^\times R^{k \rightarrow N} \Psi + \left({}^N \mathbf{r}_{Li \rightarrow Jk} \right)^\times \dot{R}^{k \rightarrow N} \Psi \quad (\text{A.6})$$

for $i = 1 : n$ and $k = 1 : i$.